AD-A257 739

‖‖‖‖‖‖‖‖‖‖‖‖‖‖‖‖‖‖

NAVAL POSTGRADUATE SCHOOL
Monterey, California

DTIC
S ELECTE D
DEC 3 1992
C

THESIS

Incorporation of a Radiation Parameterization Scheme into the
Naval Research Laboratory Limited Area Dynamical Weather
Prediction Model

by

Paul C. Stewart

September, 1992

Thesis Advisor: Teddy R. Holt

92-30708

‖‖‖‖‖‖‖‖‖‖‖‖‖‖‖‖‖‖

REPORT DOCUMENTATION PAGE

1a Report Security Classification Unclassified			1b Restrictive Markings			
2a Security Classification Authority			3 Distribution Availability of Report			
2b Declassification Downgrading Schedule			Approved for public release; distribution is unlimited.			
4 Performing Organization Report Number(s)			5 Monitoring Organization Report Number(s)			
6a Name of Performing Organization Naval Postgraduate School	6b Office Symbol (if applicable) 35		7a Name of Monitoring Organization Naval Postgraduate School			
6c Address (city, state, and ZIP code) Monterey, CA 93943-5000			7b Address (city, state, and ZIP code) Monterey, CA 93943-5000			
8a Name of Funding Sponsoring Organization	8b Office Symbol (if applicable)		9 Procurement Instrument Identification Number			
8c Address (city, state, and ZIP code)			10 Source of Funding Numbers			
			Program Element No	Project No	Task No	Work Unit Accession No

11 Title (include security classification) INCORPORATION OF A RADIATION PARAMETERIZATION SCHEME INTO THE NAVAL RESEARCH LABORATORY LIMITED AREA DYNAMICAL WEATHER PREDICTION MODEL

12 Personal Author(s) Paul C. Stewart

13a Type of Report Master's Thesis	13b Time Covered From To	14 Date of Report (year, month, day) September 1992	15 Page Count 76

16 Supplementary Notation The views expressed in this thesis are those of the author and do not reflect the official policy or position of the Department of Defense or the U.S. Government.

17 Cosati Codes			18 Subject Terms (continue on reverse if necessary and identify by block number)
Field	Group	Subgroup	word processing, Script, GML, text processing.

19 Abstract (continue on reverse if necessary and identify by block number)

This paper describes the incorporation of the Harshvardhan et al. (1987) radiation parameterization into the Naval Research Laboratory Limited Area Dynamical Weather Prediction Model. A comparison between model runs with the radiation scheme and runs without the scheme was made to examine three mesoscale phenomena along the west coast of the United States during the period 0000 UTC 02 May 1990 - 1200 UTC 03 May 1990: the land and sea breeze, the southerly surge and the Catalina eddy. In general the updated model with the radiation parameterization yielded a more accurate simulation of the layer temperatures, geopotential heights, cloud cover, and radiative processes as verified from synoptic, mesoscale and satellite observations. Subsequently, the updated model also forecast a more realistic diurnal evolution of the sea and land breeze, the southerly surge and the Catalina eddy.

20 Distribution Availability of Abstract ☒ unclassified unlimited ☐ same as report ☐ DTIC users	21 Abstract Security Classification Unclassified	
22a Name of Responsible Individual T.R. Holt	22b Telephone (include Area code) (408) 646-2861	22c Office Symbol MR/Ht

Incorporation of a Radiation Parameterization Scheme into
the Naval Research Laboratory Limited Area Dynamical
Weather Prediction Model

by

Paul C. Stewart
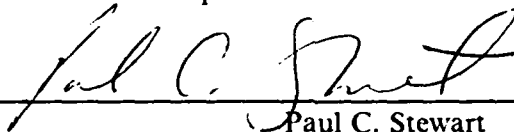Lieutenant, United States Navy
B.S., Hartwick College, 1983

Submitted in partial fulfillment of the
requirements for the degree of

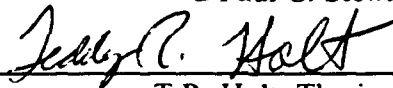MASTER OF SCIENCE IN METEOROLOGY AND PHYSICAL
OCEANOGRAPHY

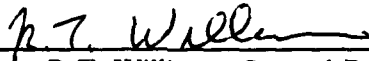from the

NAVAL POSTGRADUATE SCHOOL
September 1992

Author: _____
Paul C. Stewart

Approved by: _____
T.R. Holt, Thesis Advisor

_____
R.T. Williams, Second Reader

_____
Robert L. Haney, Chairman,
Department of Meteorology

ABSTRACT

This paper describes the incorporation of the Harshvardhan et al. (1987) radiation parameterization into the Naval Research Laboratory Limited Area Dynamical Weather Prediction Model. A comparison between model runs with the radiation scheme and runs without the scheme was made to examine three mesoscale phenomena along the west coast of the United States during the period 0000 UTC 02 May 1990 - 1200 UTC 03 May 1990: the land and sea breeze, the southerly surge and the Catalina eddy. In general the updated model with the radiation parameterization yielded a more accurate simulation of the layer temperatures, geopotential heights, cloud cover, and radiative processes as verified from synoptic, mesoscale and satellite observations. Subsequently, the updated model also forecast a more realistic diurnal evolution of the sea and land breeze, the southerly surge and the Catalina eddy.

DTIC

TABLE OF CONTENTS

ACKNOWLEDGMENTS

I. INTRODUCTION

The western United States with its coastal and topographic features creates a challenging problem for the numerical modeler. Previous studies (Grandau, 1992 ; Dorman, 1985) have examined the difficulties of modeling the marine layer off the western U.S. coast. Accurate modeling of such an area requires use of a mesoscale model that is able to resolve the topographic and coastal features. Additionally, high vertical resolution in the boundary layer is necessary to examine the air-sea interactions. One such model is the Naval Research Laboratory (NRL) Limited Area Dynamical Weather Prediction Model.

The NRL model, since its early stages in the mid-1980s, has been a continuously evolving research model that has been used to test new ideas and methods of modeling mesoscale phenomena. The NRL model has the ability to resolve the mesoscale and boundary layer features of the western United States (Grandau, 1992). In addition, the model has been shown effective with larger scale phenomena, such as rapidly deepening cyclogenesis (Holt et al., 1990 ; Schulz, 1992). The NRL model, though, has lacked an explicit radiation parameterization since it's inception.

The radiative transfer process is an extremely important factor in the western U.S. with the stratus deck normally found along the west coast. Additionally, mesoscale features, such as sea and land breezes are forced and sustained by the diurnal cycle of solar radiation. Radiative processes, latent heating, and sensible heating are not always independent, resulting in a large impact of solar radiation on the dynamics of the atmosphere in a nonlinear complex interaction. The results of the radiative processes are perceptible changes in the atmosphere. The goal of the radiation parameterization is to simulate these changes in terms of equations that represent the atmospheric forces.

Radiative processes have long been known to be strong forces in the mesoscale environment (Harrison et al., 1990 ; Stephens et al., 1990 ; Stephens, 1984). The spatial and temporal radiative changes which occur in the atmosphere result in local mesoscale forcings, especially in the oceanic environment (Schmetz et al., 1981), where the differences in albedo and air-sea fluxes are great. The stratus cloud deck can result in rapid cooling and subsequent warming as it moves in and out of an area. Additionally, the albedo can vary greatly over land as compared to over the ocean, resulting in warming of the lower atmosphere and resultant convective processes. The concept of this inter-

1

action is a key factor in the modeling of the western United States where stratus is a common occurrence in late spring and summer (Corkill, 1991), supporting the importance of an improved parameterization for radiation.

Prior to this study, the NRL model used a simplified model of radiation. The radiation parameterization scheme which is being incorporated in this study is highly vectorized allowing efficient use of computer time. Additionally, the scheme parameterizes both long and short wave radiation. Specifics about the scheme will be covered later in this paper.

The goal of this paper is to explain the incorporation of the Harshvardhan et al. (1987) radiation parameterization into the NRL model, the physics behind the parameterization and the effect of the parameterization on model performance. Additionally, the paper will examine how accurately the radiation parameterization simulates the west coast forcings and how the mesoscale features noted by Grandau (1992) are affected by the heating and cooling processes. This examination will be performed by using the model runs of Grandau (1992) without an explicit radiation scheme as a control data set and the model runs with the updated radiation parameterization as the test data set. From this point forth the Grandau (1992) model will be designated CONTR and the radiation updated model will be RAD. Graphical techniques will be used to analyze and compare the two data sets.

Chapter II describes the NRL model, the input data and satellite data. Chapter III describes the physics of the radiation parameterization and the incorporation of the radiation scheme into the NRL model. Chapter IV discusses the synoptic and mesoscale features which occurred during the time period of this experiment. Chapter V describes the results of the comparison of the two data sets. Chapter VI is dedicated to conclusions and recommendations.

II. MODEL DESCRIPTION, INPUT DATA AND SATELLITE DATA

A. MODEL DESCRIPTION

The Naval Research Laboratory (NRL) Limited Area Dynamical Weather Prediction Model is a three dimensional, baroclinic, quasi-hydrostatic, mesoscale model incorporating parameterizations for the boundary layer, convection, and radiation. Application of the model in the lower troposphere is appropriate where the balance of large scale motions is nearly gradient. The model specifics are detailed by Chang et al. (1989) and Madala et al. (1987). A brief summary follows.

1. Equations

The governing primitive equations for the model are in surface pressure weighted flux form. The seven equations consist of five which are prognostic and two which are diagnostic. The prognostic equations include the u and v momentum equations, the thermodynamic equation, the moisture continuity equation, and the surface pressure tendency equation. The hydrostatic and continuity equations are diagnostic. The seven equations form a closed set of the following dependent variables; u, v, T, q, p_s, ϕ, and $d\sigma/dt$.

2. Numerics

a. C-grid

The seven equations are then approximated using a second order accurate finite difference scheme. This type of numerical technique allows geostrophic adjustment and the separation of the higher frequency quasi-linear gravity waves from the lower frequency Rossby waves. The linearized equations are then transposed onto a C-grid (Arakawa and Lamb, 1977) to perform the horizontal finite differencing. The C-grid is chosen for its improved simulation of geostrophic adjustment and conservation of integral properties. The C-grid works best in handling this adjustment process for three reasons. First, the staggering of the grid on curvilinear horizontal coordinates is best suited to react to the small scale waves found in the post initialization process. Second, the staggered C-grid allows only the real part of the finite difference form to be calculated. Third, the grid best simulates the phase speeds associated with the propagating waves and provides a more accurate representation of the mass and wind fields.

3

Table 1. MODEL SIGMA LEVELS

Model level	Del Sigma	Sigma
1	0.1	0.05
2	0.1	0.15
3	0.1	0.25
4	0.1	0.35
5	0.1	0.45
6	0.1	0.55
7	0.08	0.64
8	0.07	0.715
9	0.06	0.78
10	0.05	0.835
11	0.04	0.88
12	0.03	0.915
13	0.02	0.94
14	0.014	0.957
15	0.01	0.969
16	0.008	0.978
17	0.006	0.985
18	0.004	0.99
19	0.003	0.9935
20	0.002	0.996
21	0.0015	0.99775
22	0.0010	0.998
23	0.0005	0.99975

Simulations with both the CONTR and RAD model employ the 23 vertical sigma levels denoted in Table 1. 13 layers below 850mb ensures high vertical resolution in the boundary layer. The horizontal domain consists of a 103 by 91 grid with constant 1/6 degree resolution in latitude and longitude from 28°- 43°N, 130°- 113°W. As in most C-grids, the geopotential, specific humidity, and temperature are calculated at the mass points (i,j). The u velocity (east-west) is calculated at the midpoint of the mass points (i,j) along the X axis; the v velocity (north-south) is calculated at the midpoint of the

4

mass points (i,j) along the Y axis and the w velocity (vertical) is computed at the mid-points between sigma surfaces.

b. Time differencing

The split explicit differencing method is used for time integration. The terms from the prognostic equations are broken into two parts governing the gravity and Rossby modes, respectively. Splitting of these equations allows integration with time steps appropriate to the individual Courant, Friedrichs, and Lewy (CFL) criteria. Chang et al. (1989) showed that this method of splitting allows use of a time interval four times that of a conventional leapfrog method.

c. Numerical Stability

A second order horizontal diffusion scheme is used with a nondimensional diffusion coefficient ($K_H \Delta t/(\Delta x)^2$) of 0.004, thus nonlinear growth is limited with minimal loss of the actual solution. This diffusion is not applied to the mixing ratio and temperature in the vertical; instead, vertical diffusion is applied on sigma surfaces.

3. Boundaries

Treatment of the boundaries in a limited area model is critical to achieving accurate results. The higher resolution achieved by a mesoscale regional model may be completely offset by poor treatment of the boundaries. The NRL model uses a temporal relaxation scheme at its' boundaries. The values five gridpoints in from the boundaries are relaxed toward the large scale analysis. The outside boundaries are then updated every 12 hours and nudged toward hourly interpolation. Chang et al. (1989) and Holt et al. (1990) supported this method versus less capable fixed, time dependent or sponge boundary schemes.

4. Parameterizations

The model contains several parameterized physical processes including convective and non-convective precipitation, dry convective adjustment, a planetary boundary layer and radiation.

The convective precipitation is parameterized by a modified Kuo scheme (Kuo, 1974). Based on moisture convergence and stability, convective precipitation is computed on the grid scale. The low level moisture convergence results in either an increase in humidity or atmospheric condensation and subsequent precipitation.

The Clausius - Clapeyron equation is used to calculate excess moisture and isobaric heating; based on this computation, non-convective precipitation can be determined. If excess moisture occurs and is above the critical value for that sigma level then

precipitation can occur. It is then determined whether this precipitation will fall into the lower levels and evaporate or fall, not evaporate completely and reach the ground.

Dry convective adjustment parameterization is used to neutralize the superadiabatic lapse rates. The method is applied just above the boundary layer when the static energy of a specific layer is greater than the next higher layer. The result of the adjustment is a stable lapse rate while conserving total static energy.

The planetary boundary layer (PBL) parameterization implements the turbulent kinetic energy (TKE) closure scheme as outlined in Holt and Raman (1988). Monin-Obokov similarity theory is used to parameterize the surface boundary layer. Due to the large gradients in topography, a constant roughness length of 5 cm was assigned over all land areas; 5 cm is generally accepted for most operational numerical weather prediction models as a good approximation to the roughness length over land. Roughness length over water was determined by Charnock's relation.

As part of the PBL parameterization, soil temperature is computed from a soil slab model (Blackadar, 1976). The soil slab model predicts the ground surface temperature based on the surface energy equation of Chang (1979).

The radiation parameterization will be discussed in detail in Chapter III.

B. INPUT DATA

The data for the period 0000 UTC 02 May - 1200 UTC 03 May 1990 is taken from the Navy Operational Global Atmospheric Prediction System (NOGAPS). A brief description of this data set follows. Data for the initialization of the model was retrieved from the archived Fleet Numerical Oceanography Center's NOGAPS 2.5 degree global analyses. Fields include u-components (u) and v-components (v) of velocity, temperature (T), vapor pressure (e), D-values, sea level pressure (SLP) and sea surface temperature (SST). The SST field was kept constant throughout the integration. These fields, with their corresponding levels are given in Table 2. Geopotential heights were computed from D-values using the NACA standard atmosphere relations (Haltiner and Martin, 1972).

Table 2.   NOGAPS GRIDDED INPUT FIELDS.

Level (MB)	Parameters
Surface	SLP, SST
1000	D-Value, u, v, e, T
925	D-Value, u, v, e, T
850	D-Value, u, v, e, T
700	D-Value, u, v, e, T
500	D-Value, u, v, e, T
400	D-Value, u, v, e, T
300	D-value, u, v, e, T
250	D-Value, u, v, T
200	D-Value, u, v, T
150	D-Value, u, v, T
100	D-Value, u, v, T
70	D-Value, u, v, T
50	D-Value, u, v, T
30	D-Value, u, v, T
20	D-Value, u, v, T
10	D-Value, u, v, T

All fields were interpolated horizontally and vertically to model resolution (Grandau 1992). Cubic polynomial interpolation was used in the horizontal; linear interpolation was used in the vertical and bilinear interpolation was used along the boundaries. Spe-

cifically, mixing ratio was interpolated exponentially in pressure; temperature was interpolated linearly in log pressure; and the u and v velocity components were interpolated linearly in pressure. Topography fields were achieved by performing 5 point averaging of the U.S. Navy global 10 minute elevation data.

C. SATELLITE DATA

Although not used in the modeling process, satellite data for the time period of this experiment was available for the analysis of the modeled runs. An entire series of IR, enhanced IR, water vapor and visible imagery was available for comparisons between the control data set and the test data set. This ground truth data, combined with the analyses of the time period, helped in making more accurate comparisons and assisted in analyzing the cloud parameterization scheme; however, exact determination of cloud type and level was very challenging by satellite imagery alone.

III. RADIATION PARAMETERIZATION

A. DESCRIPTION

The parameterization of radiation is of critical importance in order to achieve accuracy in numerical weather prediction models (Ramanathan et al., 1983); however, computation time for the model increases dramatically when a radiation parameterization is included. Therefore, there exists a trade off between accuracy and speed. In the past, radiation parameterization codes used an excess of CPU time and therefore, were called as infrequently as 5-6 hours (Stephens, 1984). This frequency of updating an atmospheric climate model was considered unacceptable and unrealistic by Wilson and Mitchell (1986) due to diurnal variations, as well as rapid changes in cloud cover and convective motion.

Clouds exert a large influence on the earth's radiational budget; thus, changes in the longwave and shortwave radiation at the surface can greatly affect the synoptic and mesoscale structure of the lower troposphere. The presence of low level stratus clouds increases the amount of downward longwave radiation at the surface, thus decreasing the longwave cooling at the surface tremendously. In addition, the albedo of the stratus deck limits the shortwave interaction from the atmosphere and surface beneath it. The cloud parameterization scheme of Slingo and Ritter (1985) has been incorporated for this study and will be discussed in detail later in this chapter.

The Harshvardhan et al. (1987) scheme incorporated here into the NRL model was developed for use in atmospheric circulation models, including regional and global models. The objective of the parameterization was to create a scheme which approximated the radiative processes as accurately as possible with the fewest radiational bands, and to develop a flux computation algorithm that could be highly vectorized. Harshvardhan et al. (1987) stressed that vectorizability is the most important factor in creating a radiation parameterization scheme that could be called with a frequency of one hour or less.

In the Harshvardhan et al. (1987) parameterization, the emmisivity and absorptance formulation are applied to water vapor, ozone and carbon dioxide to provide a simplified method for modeling the radiative processes. These methods are then applied to the lower atmosphere to achieve accurate and rapid approximations. The Harshvardhan et

al. (1987) study applies this concept to longwave and shortwave radiation and is described in detail below.

1. Longwave Radiation

The long wave calculation starts by initially calculating the longwave fluxes in the cloud free atmosphere using the broadband transmission approach of Chou (1984) for water vapor, that of Chou and Peng (1983) for carbon dioxide and Rodgers (1968) for ozone. Other gases, such as methane and oxygen are not included due to their scaled effects and the desire to keep the efficiency of the parameterization scheme to a maximum.

The vibration-rotation bands of carbon dioxide, ozone and water vapor, as well as the pure rotation bands and continuum bands of water vapor, contribute to the emmision and absorption of longwave energy within the atmosphere. Treatment of these bands in the radiative flux calculations would involve line by line integrations to model the physics perfectly; however, those integrations would be very time intensive. The general procedure, which is done in longwave as well as shortwave, is to treat the bands in terms of spectrally integrated emmisivities and absorptance formulation. This is the concept behind the three longwave broadband methods.

a. *Cloud Free Atmosphere*

In the clear atmosphere, longwave radiation is computed using the three approaches noted above. Table 3 lists the spectral regions over which the longwave radiation scheme is applied. Note that in the 5 bands, the band center and band wing regions are not contiguous in wave number thus losing some accuracy but maintaining high efficiency. Included within these bands are water vapor continuum absorption, which overlaps the line absorptions for carbon dioxide, ozone and water vapor. The continuum absorption is based on the Roberts et al. (1976) formula.

Table 3. SPECTRAL RANGES IN THE LONGWAVE SCHEME (cm^{-1})

Water Band		Carbon Dioxide Band		Ozone Band
Centers	Wings	Centers	Wings	
0-340	340-540	620-720	540-620	980-1100
1380-1900	800-980		720-800	
	1100-1380			
	1900-3000			

The concept behind the approximation is to calculate diffuse transmittance using empirical formulas. These calculations are then stored and may be recalled. These

10

computations are known as the reference conditions and represent the regions of peak cooling in the atmosphere. Chou (1984) also used relationships to approximate the transmission values of water vapor lines and continuum in the overlap regions with carbon dioxide and ozone, respectively. The parameterization incorporates this concept; however, it uses a constant region of wave number over which ozone absorptance occurs.

b. Cloudy Atmosphere

For the cloudy sky, Harshvardhan et al. (1987) introduced a probability scheme to compute a clear line of sight from the top of the atmosphere to the surface. This calculation is based on the input of grid cloud fractional data which is computed using the Slingo and Ritter (1985) cloud parameterization to be described later in this chapter. With a fractional number as input, the cloudy sky fluxes could be calculated using factors to account for the differences in cloud versus non-cloud radiation. The upward and downward fluxes are then calculated at any level and grid in the atmosphere.

2. Shortwave Radiation

The transfer of shortwave radiation is much less complex than that of longwave radiation transfer, in that it is not necessary to consider the complicated dilemma of simultaneous absorption and emission from layer to layer in the atmosphere. Therefore, the transmission function for solar radiation can be defined much more simply.

Rayleigh scattering and reflection off clouds are treated using a two-stream method to calculate fluxes over a range of atmospheric conditions. Conditions may vary continuously, including changes in cloud cover and optical depth. Therefore the cloud parameterization scheme must be called frequently to accurately approximate the atmosphere.

The shortwave calculations for this parameterization are an extension of Lacis and Hansen (1974). The absorption is computed in two wavelength bands: $\lambda < 0.9\mu m$ and $\lambda > 0.9\mu m$ where water vapor is the sole absorber in the upper band and ozone is limited to the lower band. The treatment of water vapor absorption, ozone absorption, clear sky Rayleigh scattering and the use of probability distributions to represent water vapor contribution to the extinction coefficient in the solar infrared are retained in their original form from Lacis and Hansen (1974). Changes made to the Lacis and Hansen (1974) scheme include the treatment of scattering by clouds, which was made independent of the solar zenith angle, and the specification of the cloud optical depth. Harshvardhan et al. (1987) states that given a single scatter albedo and a cloudy layer with a known optical depth, the direct reflection and transmission may be calculated

11

using the delta-Eddington (Joseph et al., 1976) or the two-stream (Coakley and Chylek, 1975) method. Based on this calculation and an improved optical depth value, more accurate reflection and transmission values are achieved.

Transmitted and reflected flux values are then calculated as functions of insulation, reflection and transmission. The parameterization sums the flux values to obtain broadband values. The overall scatter albedo of a cloud layer is then determined by combining the individual water droplet's scattering optical depths and assymetry factors. Thus, with this information, the effective water vapor absorption coefficients are found using the Lacis and Hansen (1974) k distribution.

a. k Distribution

The k distribution, a method used recently by Hansen et al. (1983) and Chou and Arking (1981) among others, is used to approximate frequency integrations in flux equations. This is accomplished by grouping frequency intervals according to line strengths. Then, by assuming a homogeneous atmosphere, it is related to the transmission function. Hansen et al. (1983) demonstrated that this method was a more accurate treatment of vertical inhomogeneities since the k distribution at all altitudes is correlated in frequency space; in other words, the strongest or weakest absorption always occurs at the same frequency at all altitudes in the atmosphere. This allows straight forward treatment of molecular absorption and the scattering by cloud droplets.

3. Comments and Limitations

The parameterization scheme is presently used in the UCLA/Goddard global climate model as well as NOGAPS; additionally, it was validated against other radiation parameterization schemes in an international intercomparison project (Intercomparison of Radiation Codes in Climate Models) (ICRCCM) (World Meteorlogical Organization, 1984). Since the parameterization uses numerical fitting to speed computations, the range of atmospheric parameters that may be modeled is limited. The upper limit on the total water vapor column is 8 g/cm^2. Carbon dioxide concentrations are fixed to 330 ppmv; however, coefficients allow up to four times that amount. Due to the wide diversity of aerosol types and sizes, a parameterization for them is not included.

B. INCORPORATION OF THE RADIATION SCHEME INTO THE NRL MODEL

Installing the Harshvardhan et al. (1987) radiation scheme into the NRL model required minor modification to the NRL model while the parameterization code required extensive modifications and additional support programs.

The Harshvardhan et al. (1987) parameterization scheme is a two dimensional model written originally for horizontal-vertical space. In this application of the model, longitudinal slices of the model domain are made. Many modifications were made to the array dimensions, calling statements and common blocks to account for this spatial arrangement. Most of the modifications were implemented in a support subroutine which called the various subprograms and subroutines to provide the required parameters.

1. Modifications to the Parameterization

All parameters, in various forms were available from the NRL model with some modification. Input and output parameters for the various subroutines are found in Table 4.

Table 4. INPUT AND OUTPUT PARAMETERS OF SUBROUTINES

Shortwave Code Parameters

Input	Output
number of layers	layer heating rate
layer pressure(mb)	layer absorption
layer temperature	surface absorption
layer water vapor mixing ratio	
layer ozone mixing ratio	
albedo	
cosine of solar zenith angle	
solar constant	
cloud fraction	

Longwave Code Parameters

Input	Output
number of layers	layer heating rate
layer pressure(mb)	upward flux at surface
layer temperature	upward flux at top of model
layer water vapor mixing ratio	
layer ozone mixing ratio	
cloud fraction	

Cloud Fractional Code

Input	Output
relative humidity	cloud fraction
cloud top temperature	
precipitation rate	
sigma level	

Ozone Code

Input	Output
layer pressure	ozone mixing ratio
sine of the latitude	
julian date	
time of day	

Sigma surfaces were changed to millibars for use in the radiation code; cloud top temperatures were calculated, based on a psuedo-adiabatic scheme; layer temperatures and specific humidities were averaged over the respective layers; and unit conversions were made. Additional parameters needed to support the radiation package included cloud fraction data and ozone mixing ratios.

a. Cloud Parameterization

Many crude radiational models assume longwave cooling rates within clouds based on black body theory; however, this concept assumes that the cloud is wholly contained within a grid or layer. In the Harshvardhan et al. (1987) model, this is not the case. The NRL model computes cloud fractions explicitly based on relevant meteorlogical parameters to create a more realistic distribution of clouds. This concept gives the model a much greater advantage over less sophisticated models, and allows the model to compute transmittance and absorptance with greater efficiency.

Cloud fractions are computed using a modified Slingo and Ritter (1985) method which produces stable and convective cloud fractions for a horizontal grid. The Slingo and Ritter (1985) cloud parameterization is an empirical formulation developed for the European Centre for Medium-Range Weather Forecasts (ECMWF). This method was applied to the domain area and cloud fractions of each grid at all sigma layers were produced. A brief description follows.

At each sigma layer, σ_k, two types of clouds are diagnosed; stratiform and cumulus. A critical relative humidity value, Rh_k^c, is calculated by the following equation;

$$Rh_k^c = 1 + 2(\sigma_k^2 - \sigma_k) + \sqrt{3}\sigma_k(1 - 3\sigma_k + 2\sigma_k^2) \tag{3.1}$$

where k varies from 1 to 23 representing each level in the model. The critical relative humidity values generated by (3.1) are given in Figure 1.

The critical relative humidity is compared to the average layer relative humidity, given in (3.2) to determine if saturation has occurred.

$$\overline{Rh}_k = 0.5Rh_k + 0.25(Rh_{k-1} + Rh_{k+1}) \tag{3.2}$$

where model top and bottom boundary conditions are;

$$\overline{Rh}_1 = Rh_1, \quad \overline{Rh}_H = Rh_H$$

If clouds are determined to exist, they are classified initially as stratiform using (3.3);
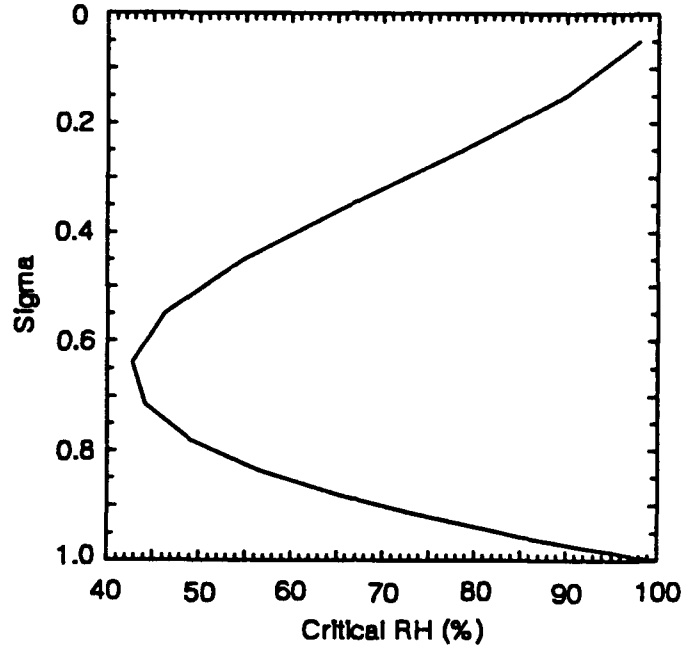
14

Figure 1. **Critical Relative Humidity (Slingo, 1985)**

$$C_{st_k} = \frac{(\overline{Rh}_k - Rh_k^c)}{(1 - Rh_k^c)^2} \qquad (3.3)$$

The cumulus cloud fraction is then assumed to begin at the lifted condensation level (LCL) and extend vertically to the highest entraining cloud level. The fraction of cumulus clouds is held constant to the level where cumulus anvils are diagnosed ($T_k \leq 233.16$) and then increased above this level to account for the horizontal extension of the ice anvil. The maximum amount that a cumulus cloud without anvils may cover a grid is 0.80 and then up to 1.00 with anvils. Ice anvil presence is determined by cloud top temperature.

The cumulus cloud fraction, C_{cu_k}, based on the amount of cumulus rainfall P_{cu} in cm/hr is defined by (3.5) and (3.6);

$$C_{cu_k} = 1.13 + 0.124 ln P_{cu}, \quad for \ T_k \leq 233.16 \qquad (3.5)$$

$$C_{cu_k} = 0.93 + 0.124 ln P_{cu}, \quad for \ T_k > 233.16 \qquad (3.6)$$

The probability, P_k, of a clear line of sight through a layer with cloud fraction, C_k is given by;

$$P_k = 1 - C_k \tag{3.7}$$

The total cloud fraction of a grid is given by the combination of the stratiform fraction and the cumulus fraction, assuming independent probabilities, in the following equation;

$$C_{T_k} = C_{st_k} + C_{cu_k} - C_{st_k} C_{cu_k} \tag{3.8}$$

This total cloud fraction is then computed over the entire domain of the model to provide the required fractions for the radiation parameterization.

b. Ozone Mixing Ratios

Geophysical Fluid Dynamics Laboratory (GFDL) data was parameterized into a code used for the Australian Global Climate Model to determine ozone mixing ratios in the atmosphere. This code was then used with modification to produce ratios for the domain of this experiment.

c. Soil Parameterization

(1) *Shortwave Radiation.* The soil parameterization used in the CONTR model was based on the work of Chang (1979). The incoming solar radiation is parameterized a function of the precipitation rate, solar zenith angle and albedo. This parameterization assumed a 39% absorption rate of the incoming shortwave radiation at the surface. This value of shortwave warming was then used to modify the ground temperature. This assumption was accurate and good results were acheived (Grandau, 1992).

For the RAD model the inc .ng shortwave radiation is calculated in the parameterization and explicitly used in the soil parameterization as the absorbed energy. This method should be more accurate than the constant absorption figure used previously since cloud cover is accounted and individual areas of surface heating are possible, thus leading to the possibility of convective activity.

(2) *Longwave Radiation.* The ground temperature for the CONTR model was modified by longwave emmision based on the blackbody assumption. The Stefan - Boltzman equation was used to calculate this value. For the RAD model the radiation parameterization calculates the net upward flux at the surface and this value is used explicitly to modify the surface temperature.

2. Implementation of the Parameterization

Once all the changes were made to the radiation parameterization, it was tested and debugged in the NRL model to ensure stability and reliability of the results. Addi-

tionally, the cloud parameterization was tested and compared to satellite imagery to ensure resonable approximations. Then, with the parameterizations tested and run, the NRL model was integrated out to 6 hours. This initial run was compared to observations and analysis fields to check for accuracy. When these initial stages of testing were completed, the NRL model was run with the radiation parameterization installed and called every 30 minutes.

IV. SYNOPTIC AND MESOSCALE FEATURES

A. SYNOPTIC SETTING

1. Upper Air Analysis

During the experiment period 0000 UTC 02 May 1990 to 1200 UTC 03 May 1990, a high pressure ridge was forming in the eastern Pacific. Figures 2, 4, 6, and 8 show the 500 mb analyses for the time period. Note the slow intensification of the 500mb ridge throughout the period. The upper level ridge resulted in northerly flow along the California coast throughout the period, slowly increasing in strength. Note also in the 500 mb analyses the closed low pressure cell over southwestern Arizona which deepened slightly in the first twelve hours then began to fill in the second and third twelve hour periods. The low center then gradually moved eastward into New Mexico and Texas. Of interest is the thermal trough seen in the northwest at the beginning of the period, indicative of a short wave disturbance in the synoptic pattern.

2. Surface Analysis

Examining the 1000 mb analyses found in Figures 3, 5, 7, and 9 reveals a closed high pressure cell off the California coast at the beginning of the period. Throughout the period the cell elongates, weakens and moves northeast. A weak low pressure system over Arizona remains stationary and fills slightly throughout the period. A weak low pressure cell begins to develop in the central Pacific and moves northeast deepening as it progresses, reaching the coast of British Columbia by the end of the period. Additionally, a high pressure ridge begins to develop in the central plain states moving northward into the Dakotas by the end of the period.

Figure 2. 0000 UTC 02 May 1990 NOGAPS 500mb Analysis: Heights (m, solid) and temperature (°C, dashed)

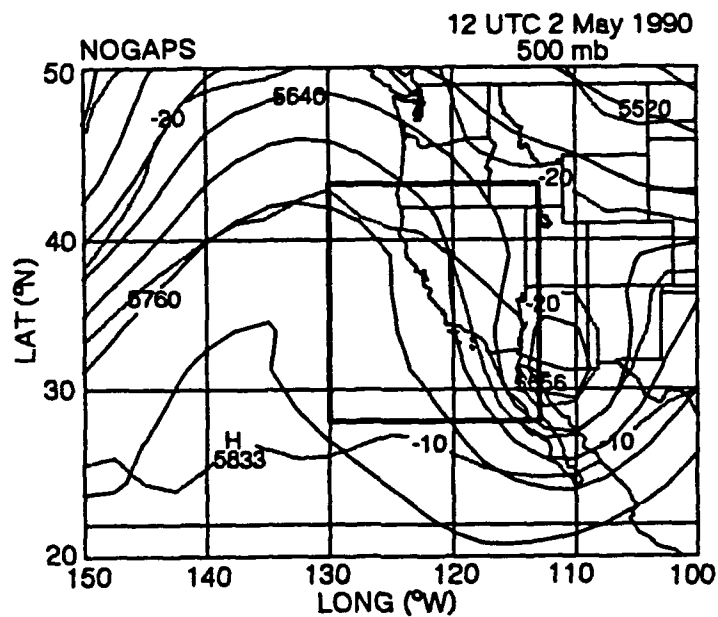**Figure 3.** 0000 UTC 02 May 1990 NOGAPS Sea Level Pressure (mb) Analysis

19

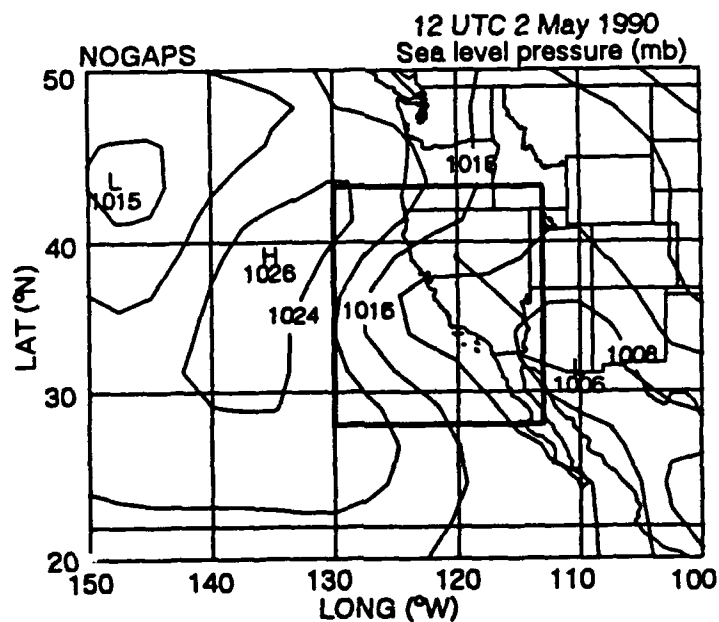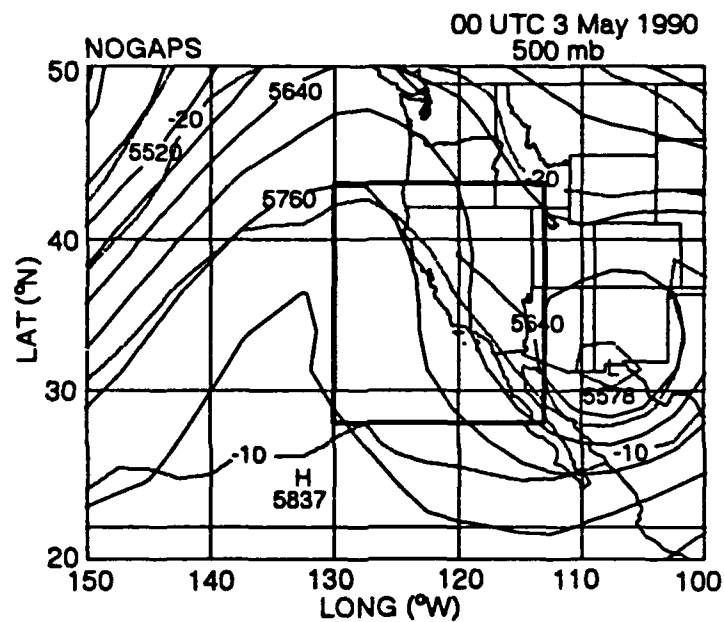**Figure 4.** 1200 UTC 02 May 1990 NOGAPS 500mb Analysis: Heights (m, solid) and temperature (°C, dashed)
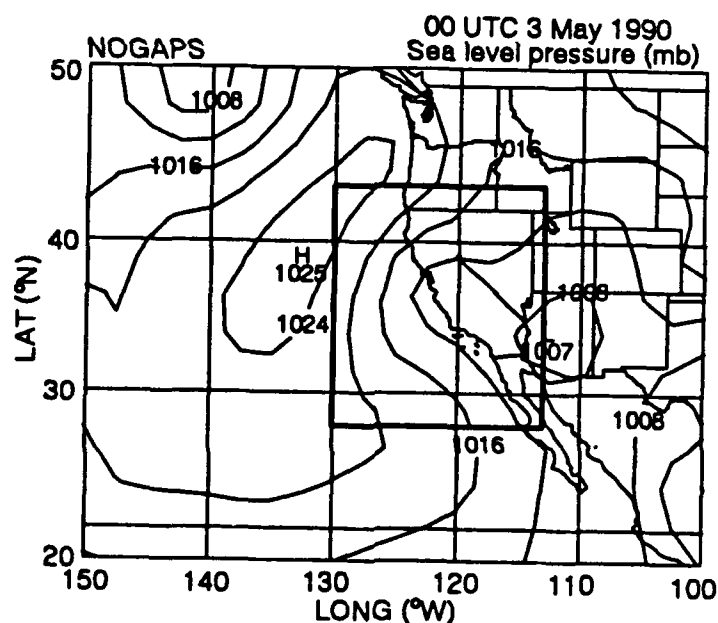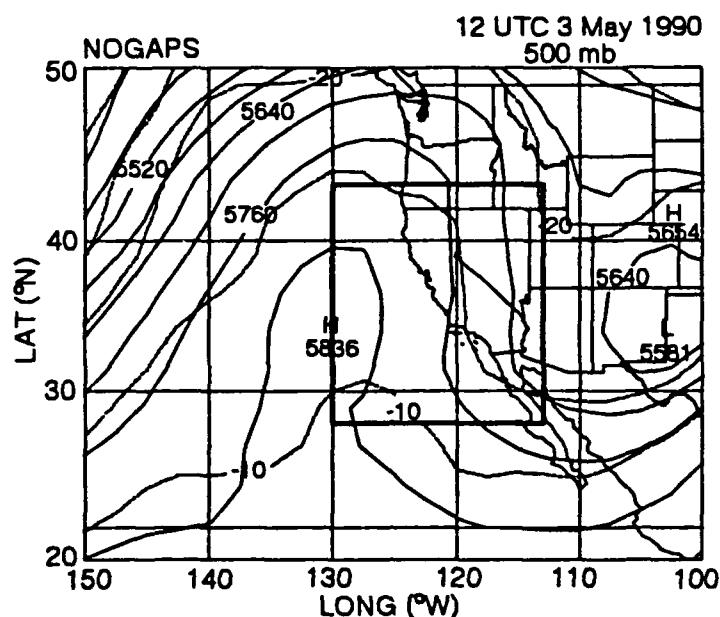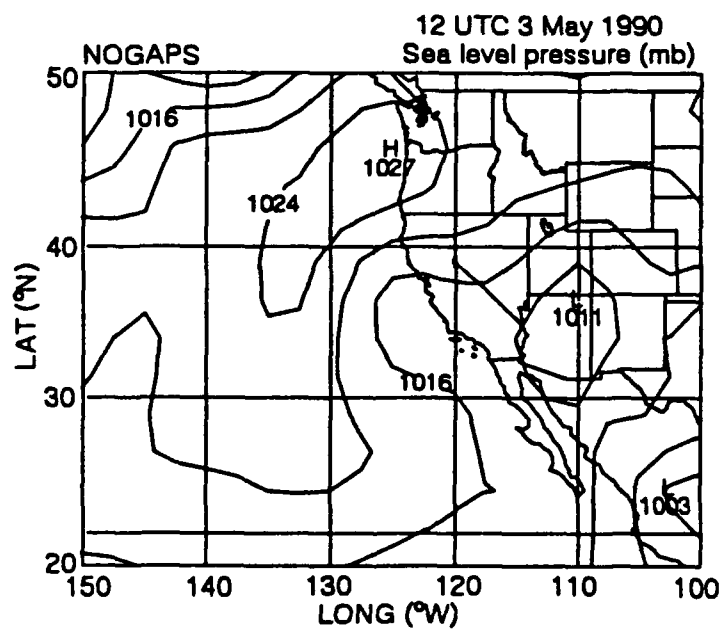

Figure 5. 1200 UTC 02 May 1990 NOGAPS Sea Level Pressure (mb) Analysis

Figure 6. 0000 UTC 03 May 1990 NOGAPS 500mb Analysis: Heights (m, solid) and temperature (°C, dashed)

Figure 7. 0000 UTC 03 May 1990 NOGAPS Sea Level Pressure (mb) Analysis

Figure 8. 1200 UTC 03 May 1990 NOGAPS 500mb Analysis: Heights (m, solid) and temperature (°C, dashed)

Figure 9. 1200 UTC 03 May 1990 NOGAPS Sea Level Pressure (mb) Analysis

22

3. Satellite Analysis

Figures 10, 11, 12, 13 and 14 are the infrared satellite series of the period 0000 UTC 02 May 1990 to 1200 UTC 03 May 1990. The synoptic features noted above are also observed in this infrared series. The high pressure ridge over the central east Pacific is evident as weather patterns are forced northeastward over the ridge. The enhanced infrared images (Figures 11 and 14) clearly show the convective activity over Arizona and off the coast of British Columbia. The visible images, (Figures 15 and 16) suggest northerly winds along the west coast. These satellite images along with the analysis from the time period greatly enhance the understanding of the synoptic situation during this experiment.

Figure 10.   0031 UTC 02 May 1990; IR Satellite Image

Figure 11.   1201 UTC 02 May 1990; Enhanced IR Satellite
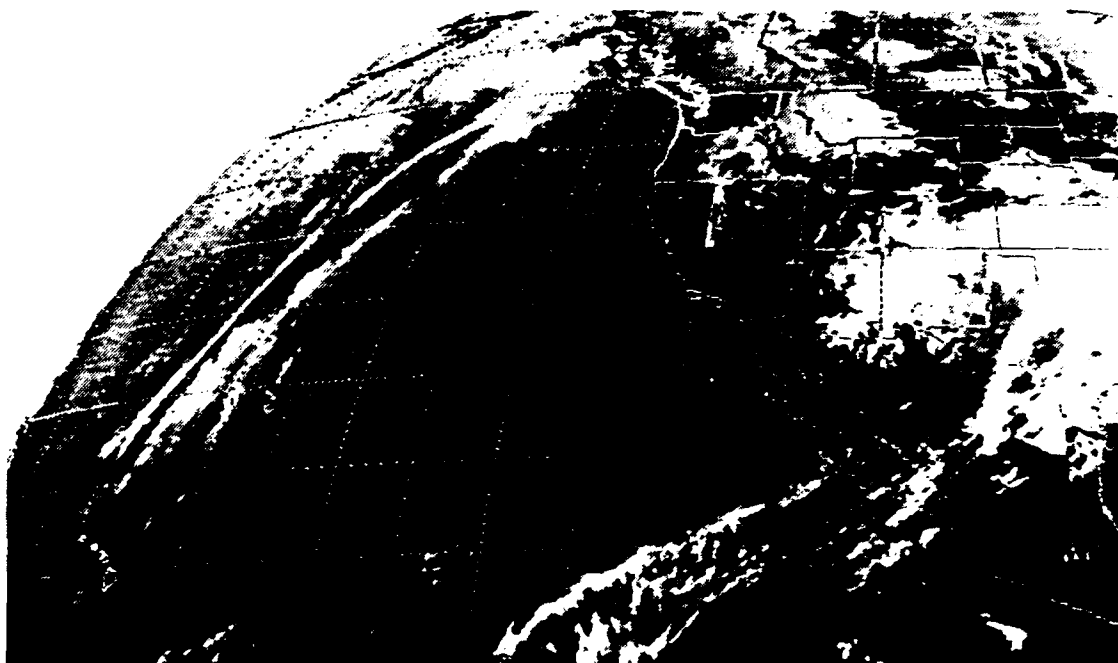Image

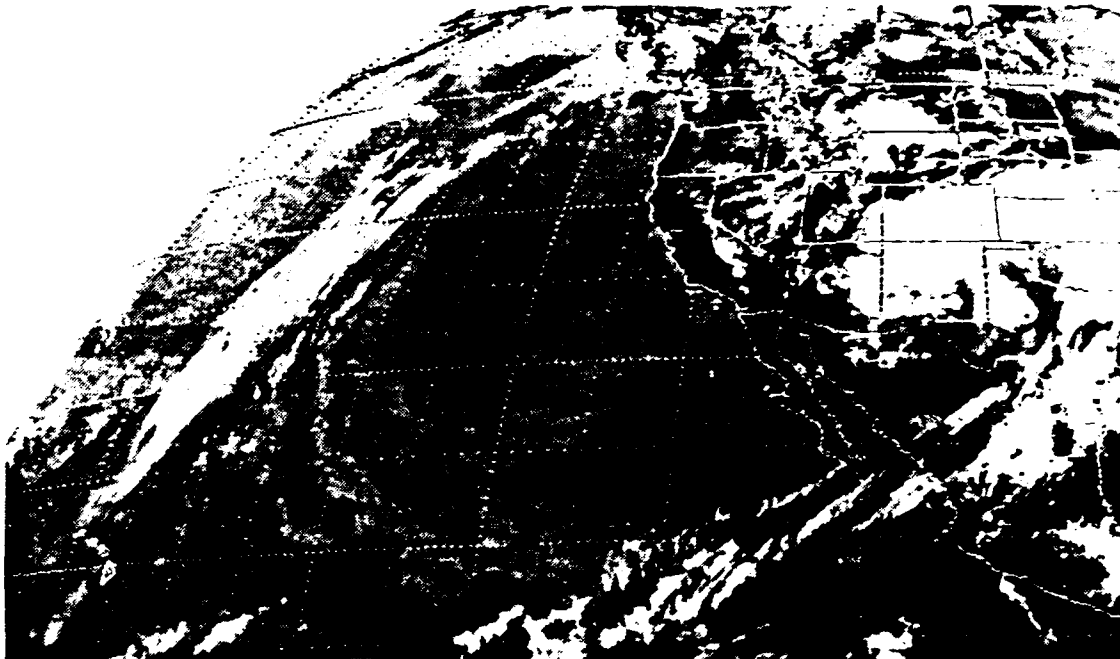Figure 12.   1731 UTC 02 May 1990; IR Satellite Image

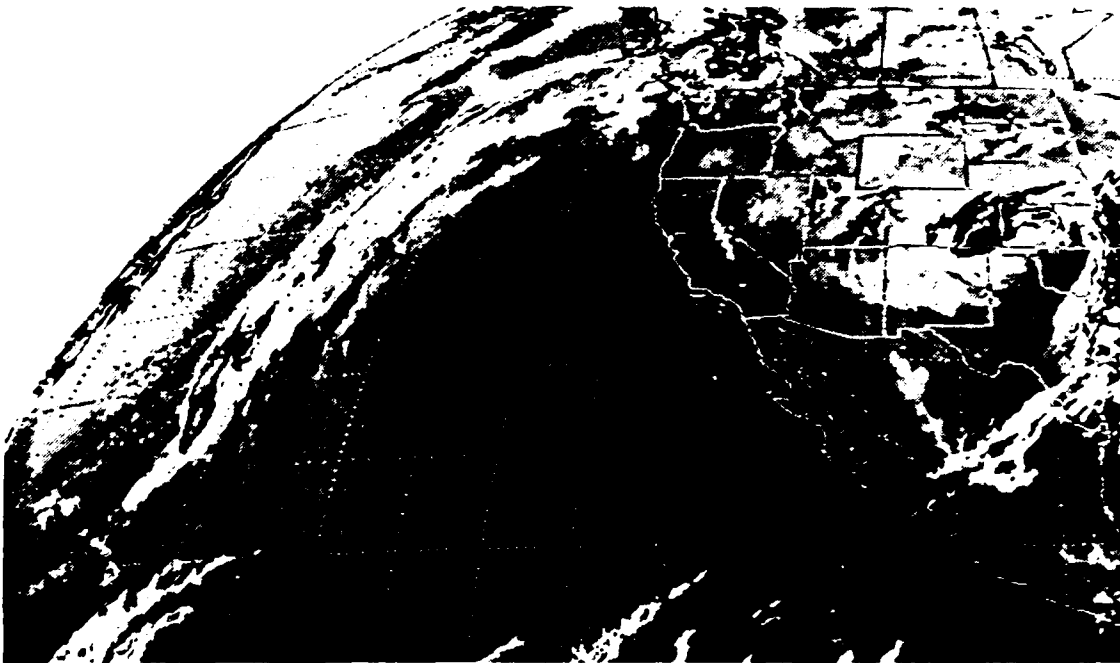Figure 13.   0031 UTC 03 May 1990; IR Satellite Image

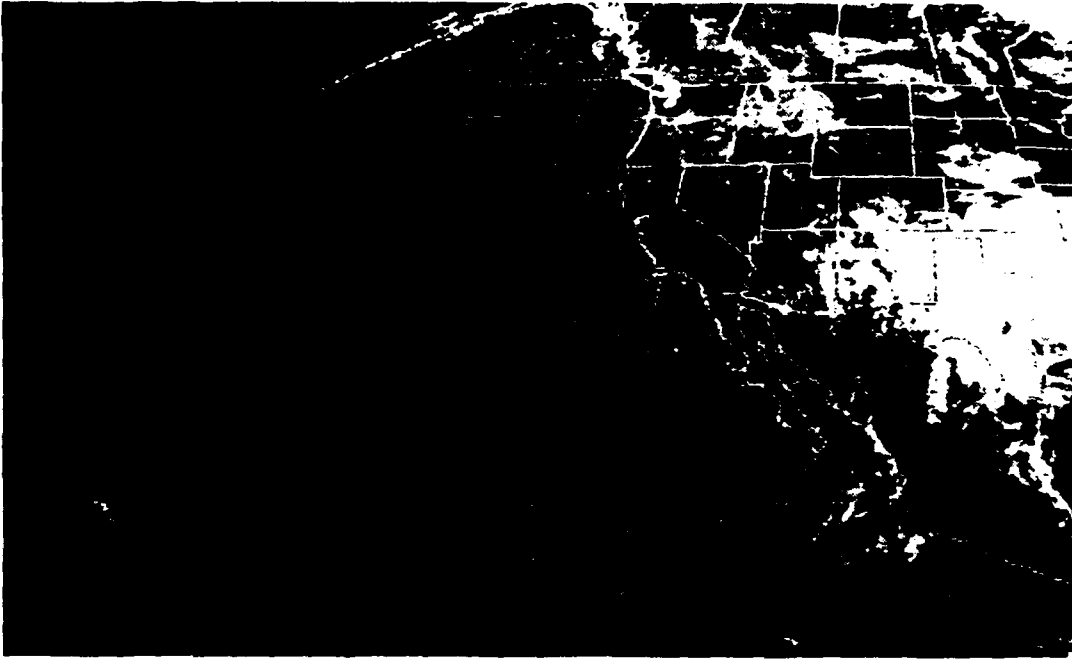Figure 14.   1201 UTC 03 May 1990; Enhanced IR Satellite
Image

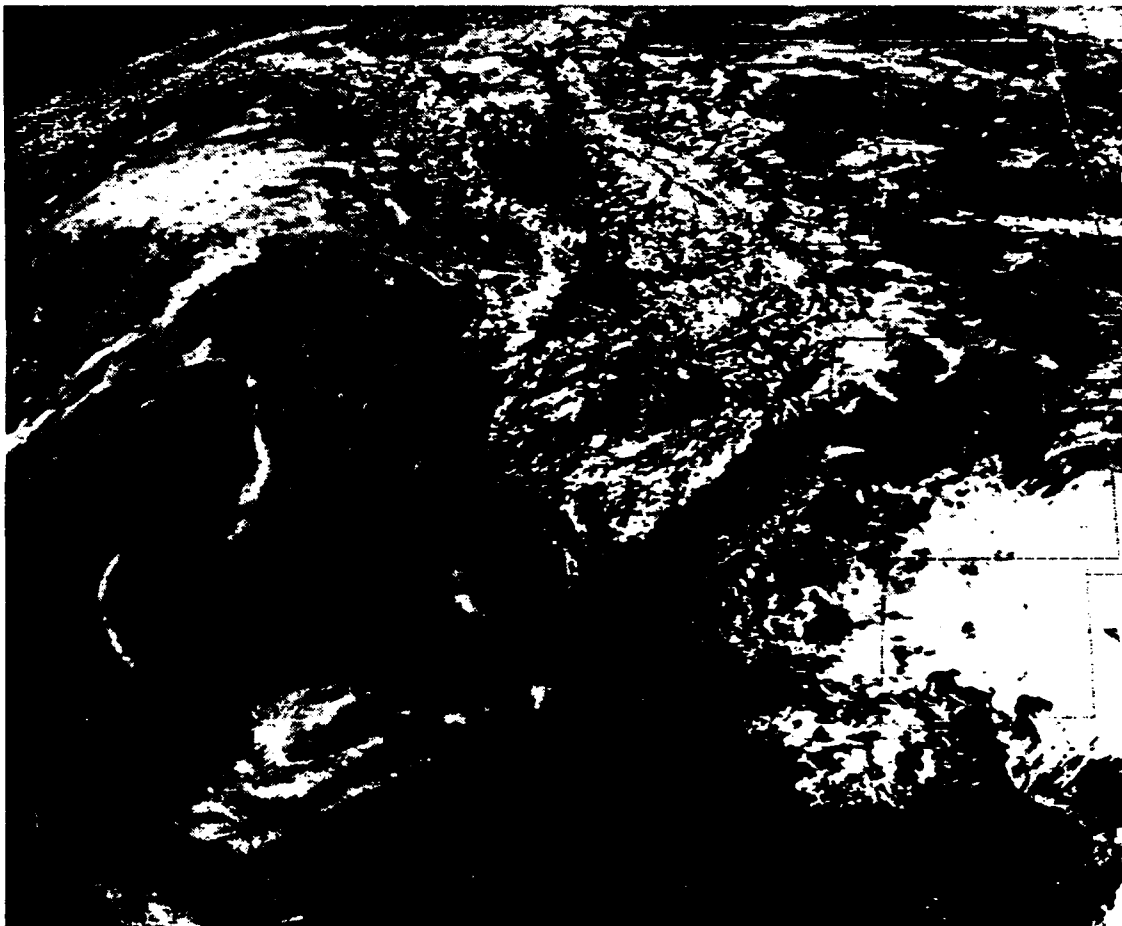**Figure 15.** 1501 UTC 02 May 1990; Visible Satellite Image

Figure 16.   2031 UTC 02 May 1990; Visible Satellite Image

B.   MESOSCALE SETTING

Three significant mesoscale phenomena were observed and documented during the period 0000 UTC 02 May 1990 to 1200 UTC 03 May 1990: the land and sea breeze, southerly surging, and the Catalina eddy. A brief description of each follows.

1. The Land and Sea Breeze

The diurnal cycle of onshore (sea) and offshore (land) breezes is forced by the heating and subsequent cooling of the land surfaces resulting in a temperature gradient across the land-marine boundary. This gradient normally results in a flow across the land - marine boundary; however, the coastal topographic features along the western United States limit the areas where land breezes can occur. The Salinas Valley is one of those areas which permits a land breeze; thus, due to the NW-SE orientation of the valley, the v-component of the wind is used here to examine the land breeze.

Streed (1990) documented the land and sea breeze during the period of this study using the NPS UHF Doppler wind profiler located at Fort Ord, CA. The observed land breeze may be seen in Figure 17 where the v-components of the wind are observed with a southerly maximum at 1200 UTC 02 May and 1200 UTC 03 May as the flow is channeled up the Salinas Valley. The observed sea breeze may also be seen in the u-component (Figure 18) with a local westerly maximum at 0000 UTC 02 May and 0000 UTC 03 May.

Streed (1990) observed and Grandau (1992) modeled the vertical structure and intensity of the land and sea breeze which was contained to the lowest 2500 meters of the atmosphere. The return flow was indistinguishable; however, as seen in Figure 18, the lower outflow is very clear and continued from 2100 UTC 02 May to 0300 UTC 03 May. The land breeze is observed from 0400 UTC 02 May 1990 to 2000 UTC 02 May 1990 in a topographically forced southerly flow in the Salinas River valley.
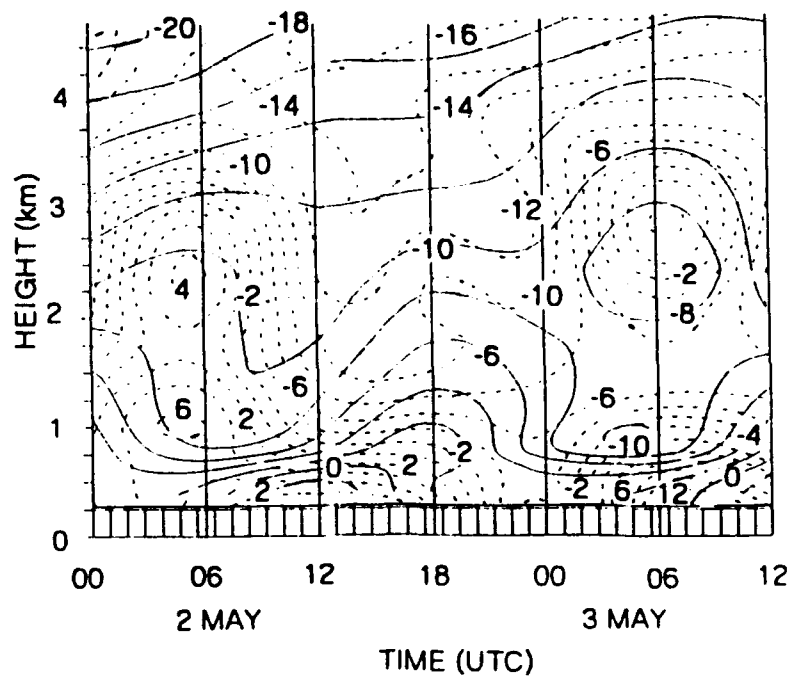
Figure 17. Time-Height Cross Section of Ft. Ord Profiler: Model (solid) and observed (dashed) v-component winds (ms^{-1})
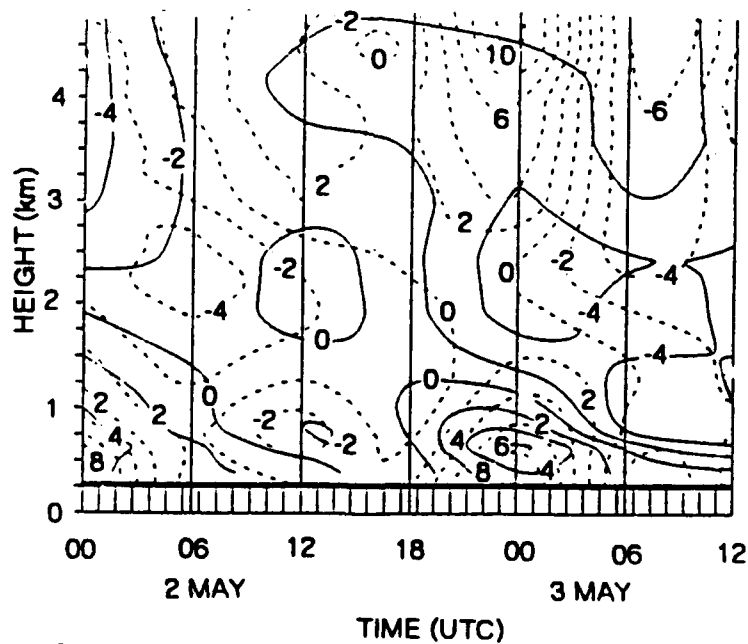

Figure 18. Time-Height Cross Section of Ft. Ord Profiler: Model (solid) and observed (dashed) u-component winds (ms^{-1})

29

2. The Southerly Surge

The stratus and fog feature which was documented by Corkill (1991) during the period 0000 UTC 02 May 1990 to 1200 UTC 03 May 1990 also describes the southerly surge feature seen in other analyses. Corkill (1991) described a low pressure system centered in central California associated with the thermal trough discussed earlier. Off-shore the flow was northerly, while southerly flow occurred along the coast resulting in a topographically forced mesoscale southerly surge. Mass et al. (1989) presented the argument that the summmmer time marine layer southerly surges occured based on the result of a coastally trapped two layer mesoscale marine system forced from the synoptic environment. Dorman (1985) documented that coastally trapped gravity currents resulted in this southerly surge. The surge is evident in the visible satellite image (Figure 16) in the vicinity of San Diego where the cloud patterns suggest southerly flow.

3. The Catalina Eddy

Mass and Albright (1989) studied topographically trapped surges in the same domain as this study. They found that the Catalina eddy was a direct result of these topographic forcings. They concluded that topographically trapped synoptic patterns led to the Catalina eddy. A synoptic scale short wave trough interacted with pre-existing troughs resulting in an intensified lower tropospheric pressure gradient. This alongshore pressure gradient causes opposing north-south flow, resultant cyclonic vorticity, and an offshore low pressure center. The resultant eddy can be supported by the synoptic pattern for long periods. Grandau (1992) observed the Catalina eddy throughout the period of this study, finding a closed vortex extending from the surface to 920mb. Low level winds simulated by the CONTR model depict this flow pattern. In addition, the visible satellite image (Figure 16) shows the cloud pattern rotation near Catalina.

V. RESULTS

A. IMPACT OF RADIATION PARAMETERIZATION ON MODEL PERFORMANCE

1. General

The RAD model parameterization was integrated for 36 hours over the period 0000 UTC 02 May 1990 to 1200 UTC 03 May 1990. Integration was over the same domain and time period as the CONTR model of Grandau (1992) thereby allowing worthwhile comparisons between the two simulations. The synoptic and mesoscale patterns from each of the model runs will be the basis for comparisons.

The diversities in the synoptic pattern over the 36 hour integration period also gives rise to coastally induced mesoscale features which have been discussed in previous chapters and will be a foundation for comparison of the two model runs.

The evaluation between the two model runs was primarily concerned with layer temperature fields, geopotential height fields, longwave and shortwave heating rates, variations introduced due to the cloud parameterization, and precipitation. Comparison of the model output from both the RAD and CONTR models was made in each of these areas.

Model output was available every 6 hours and the two model runs were compared at each of these time increments; however, since observations were available at 12 hour increments and for the brevity of this study only the 12, 24, and 36 hour comparisons were transcribed.

The two model runs were compared using the Naval Postgraduate School Interactive Digital Environmental Analysis (IDEA) Lab General Analysis (GENAL) software package. Three different methods were used to examine the two simulations. First, visual and difference field comparisons were made of the 23 layers noted in Table 1. Second, cross sections, difference fields and profiles were made at various critical locations within the model domain. Third, due to the relative effects of the radiation package, 9 levels from the surface to 900mb and any levels which contained clouds were examined closely to analyze the radiative and cloud related effects.

The differences between the two model runs were not large; however, there were several subtle, significant differences, which resulted in an altered synoptic and mesoscale pattern. The RAD model with the radiation parameterization yielded a more accurate

simulation of the layer temperature, geopotential heights, radiative processes, cloud cover and precipitation. These basic differences between the two models are examined here to understand their effects on the mesoscale phenomena discussed earlier.

a. Layer Temperature

In comparing the two model runs, examination of the layer temperature profiles in the vicinity of the low level cloud tops was made with the following results. Layer temperatures of the RAD model in the layers adjacent to the cloud tops were generally between 1.5°C and 2°C lower than those found in the CONTR model. Figure 19 is the horizontal plot of the points of interest which will be referred to for all profiles and cross sectional plots in this paper. Figure 20 is the 960mb horizontal temperature difference field of the RAD - CONTR models at 1200 UTC 03 May. 960mb was generally the level of the cloud tops 130km offshore from San Diego. Figure 21 is the temperature profile at point D containing a layer of stratus clouds between 1000mb and 960mb. Note the cooler trend of the RAD model from the cloud top upwards. These differences noted at the cloud tops are not seen in the cloud free areas, thereby confirming the longwave radiative effects at the cloud tops. The upper level clouds (400mb-250mb) found in the northwest quadrant had significantly lower differences between the two models. This is believed to be the response to the lower liquid water content of the upper level clouds. The high liquid water content of the low and mid-level clouds results in a greater longwave cooling from the cloud tops.

Figure 22 is the 1000mb temperature difference field of the RAD - CONTR models at 1200 UTC 03 May, which is the bottom of the cloud layer. It is interesting to note that the cooler air mass from above the cloud layers is advected by the northwesterly mean wind, and subsides in an area 30 km off the coast of San Diego, CA. This result may be observed in Figure 22 where the RAD model temperatures are 2°C lower than the CONTR model in the vicinity off San Diego. This result is significant and will be discussed later.

During the daylight hours when shortwave radiation is important, only slight changes to the longwave radiation are seen near cloud top. Since the cloud temperatures are not changed significantly by the shortwave radiation, compared to the longwave radiational effects, the thermal output does not change much and the layer temperature differences remain fairly consistent throughout the 36 hour period.
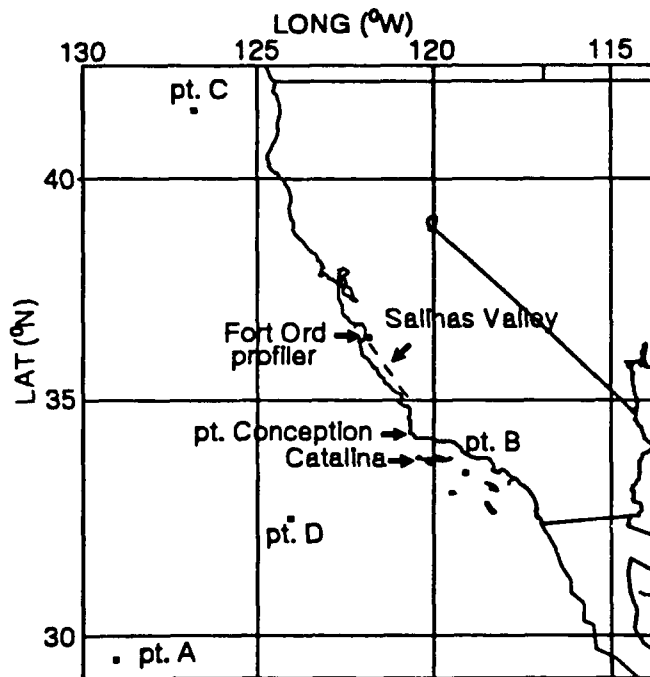
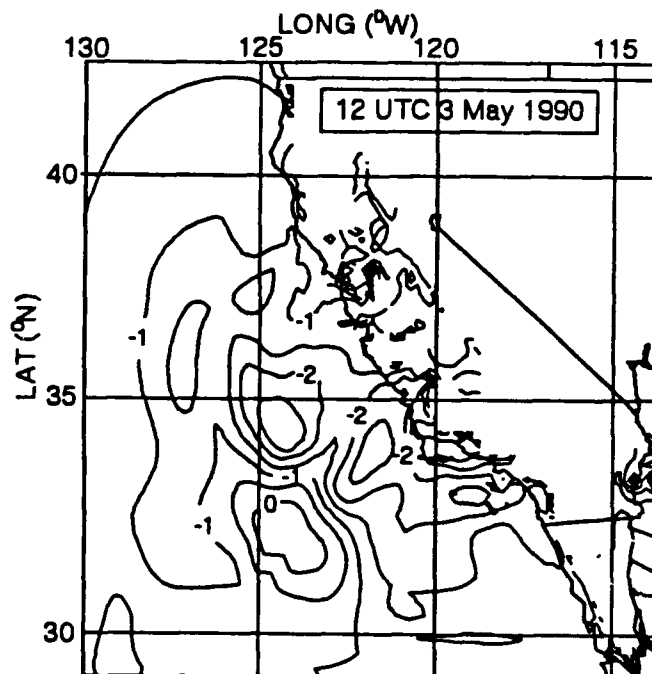**Figure 19.** Horizontal Plot of Points of Interest

Figure 20. 960mb Layer Temperature Difference (°C): RAD minus CONTR, 1200 UTC 03 May 1990
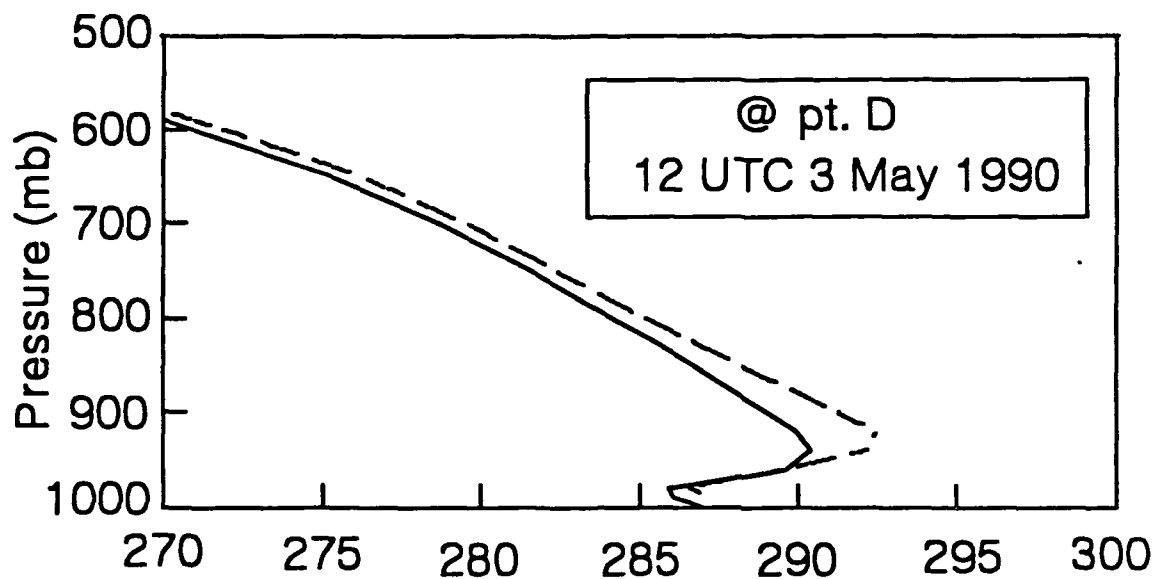
33

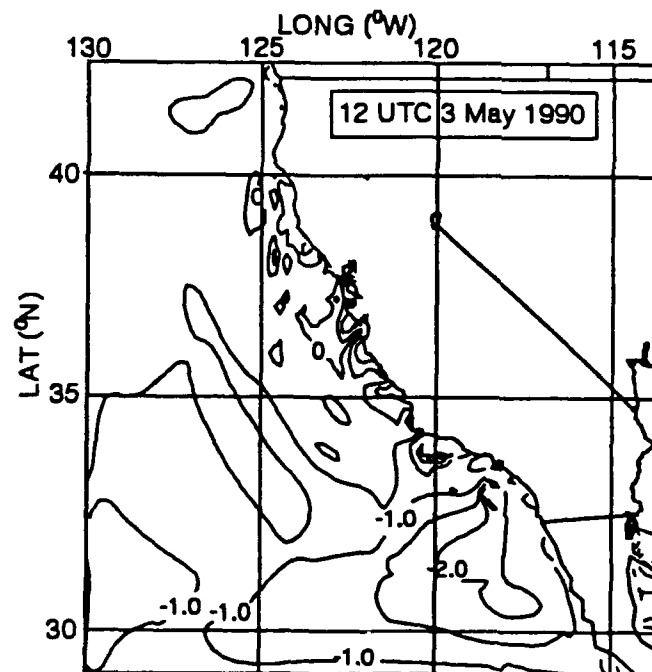**Figure 21.** Temperature Profile: (solid; RAD model, dashed; CONTR model), 1200 UTC 03 May 1990

Figure 22. 1000mb Layer Temperature Difference (°C): RAD minus CONTR, 1200 UTC 03 May 1990

b. *Geopotential Heights*

Figure 23 is a horizontal plot of the 1000mb geopotential height fields of the RAD and CONTR models at 0000 UTC 03 May 1990. Note the general increase in the difference value between the two height fields from west to east towards the west coast. The RAD model is approximately 10 meters higher just off the coast of Los Angeles in the vicinity of the stratus clouds. This increase of the near surface geopotential height fields is a direct result of the temperature differences found in the cloud layers as the radiation is emmitted out the top of the column. Note to the northwest in the model domain that the height falls are not found, indicating less temperature change in that area.

Figure 24 is the horizontal plot of the 1000mb geopotential height fields at 0000 UTC 03 May using a contour interval of 5 meters which highlights the ridging seen in the southeast area of the model domain. As seen in the CONTR model 0000 UTC 03 May 1000mb geopotential height field (Figure 25), the ridging is not observed. This feature of ridge building in the RAD model continues throughout the first 24 hour period.

In the final 12 hours of the RAD model run, the ridge tends to weaken which is a result of the cooler advected air from the cloud tops subsiding and causing height falls in the vicinity of the ridge.. The CONTR model does not support any ridge development in this area.
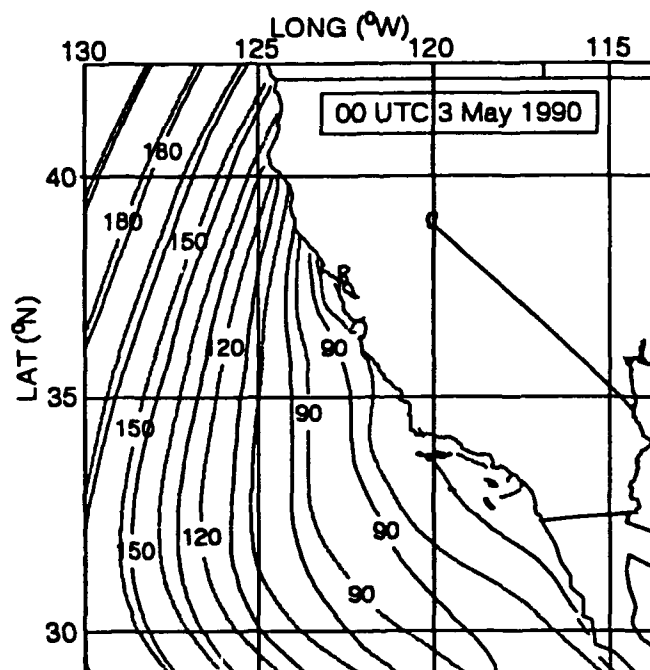
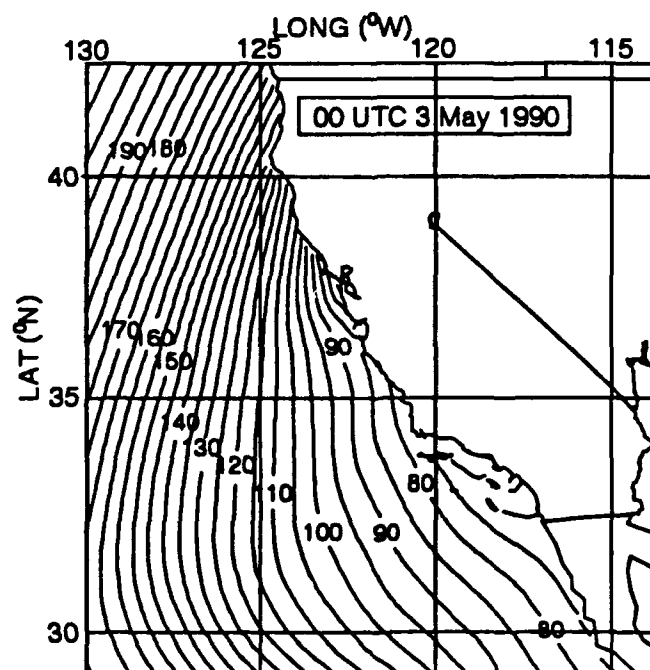**Figure 23.** 1000mb Geopotential Height Fields (solid; RAD model, dashed; CONTR model), 0000 UTC 03 May 1990

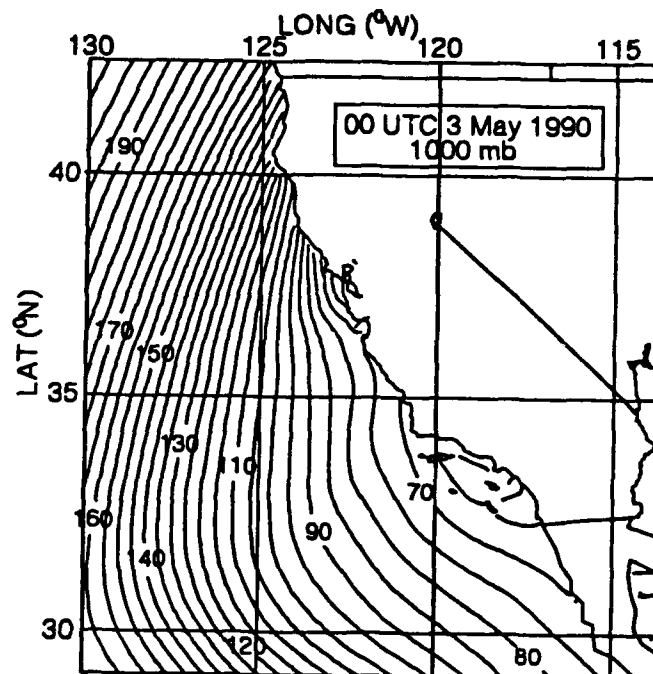**Figure 24.** 1000mb Geopotential Height Fields: 0000 UTC 03 May 1990, RAD Model

Figure 25. 1000mb Geopotential Height Fields: 0000 UTC
03 May 1990, CONTR Model

c. Longwave Radiation

The first 12 hours (1600 LST - 0400 LST) of the model's integration are primarily without solar radiation playing a factor; therefore, the longwave cooling was initially examined as the key factor for differences between the two models. Figure 26 is the cross section of longwave cooling from point A to point B. This cross section is typical of the longwave cooling structure of the low level clouds found in the RAD model domain throughout the 36 hour period with the maximum of longwave cooling near cloud top and longwave warming near the surface. Figure 27 is a profile at point D within one of the thicker layers of stratus in the southwestern quadrant. The longwave cooling rates seen here are typical of nocturnal cloud top cooling rates of low level stratus clouds (Estournal and Guedalia, 1985). Notice that the maximum value occurs near cloud top and above this level longwave cooling is near 0°C/ day. Figure 28 is a cross section of the potential temperature as related to the cloud fractions from point A to point B. The entire atmospheric temperature pattern is affected by the longwave cooling from cloud tops as seen here. These results are fairly consistent throughout the period with minor changes in the vertical and horizontal structure of the

longwave cooling patterns. These structure variations are due to changes in the cloud fractional patterns and will be discussed later.

The CONTR model does not account for longwave cooling in the atmosphere and thus this feature can not be compared between the two model runs.
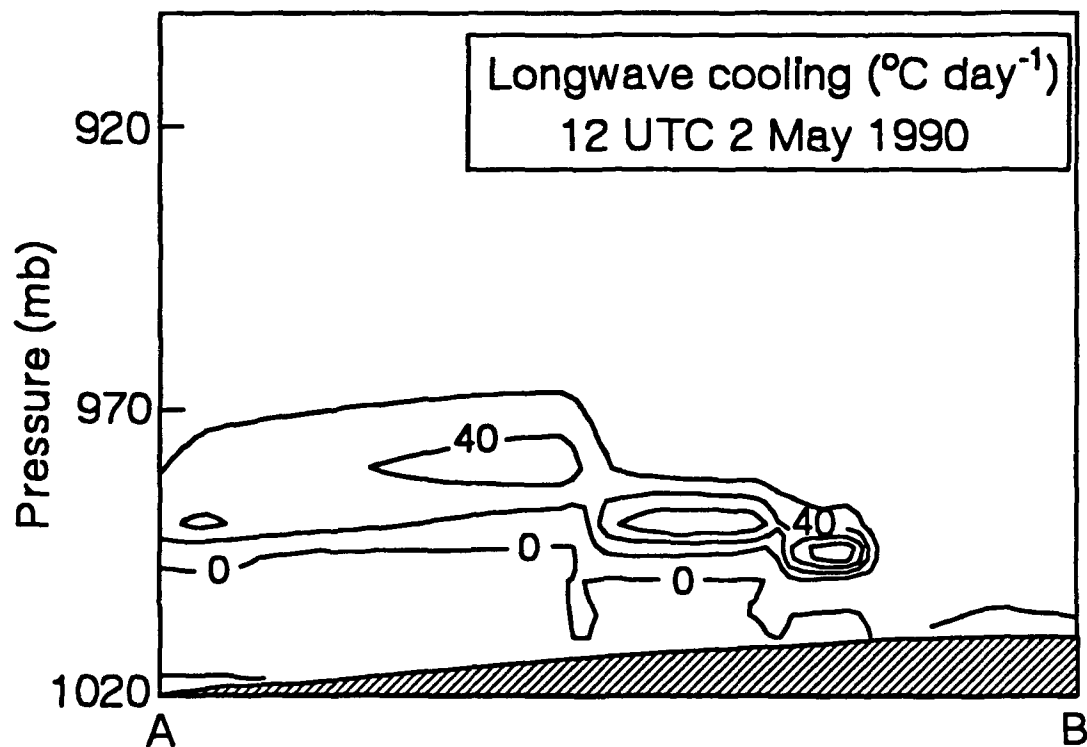

Figure 26. Cross Section of Longwave Cooling (°C/day): from point A to point B, 1200 UTC 02 May 1990
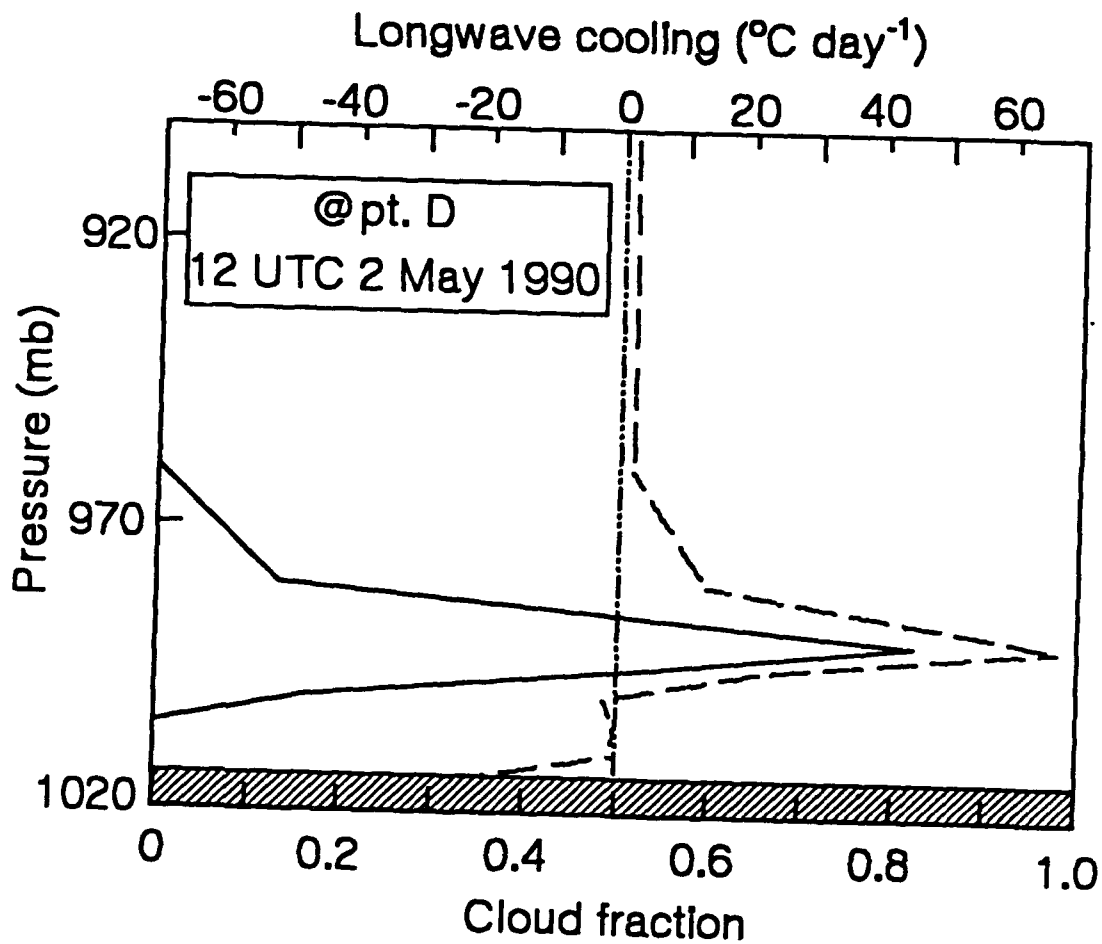
Figure 27. Profile of Longwave Cooling (°C/day) and Cloud Fractions: (solid; cloud fraction, dashed; longwave cooling), 1200 UTC 02 May 1990
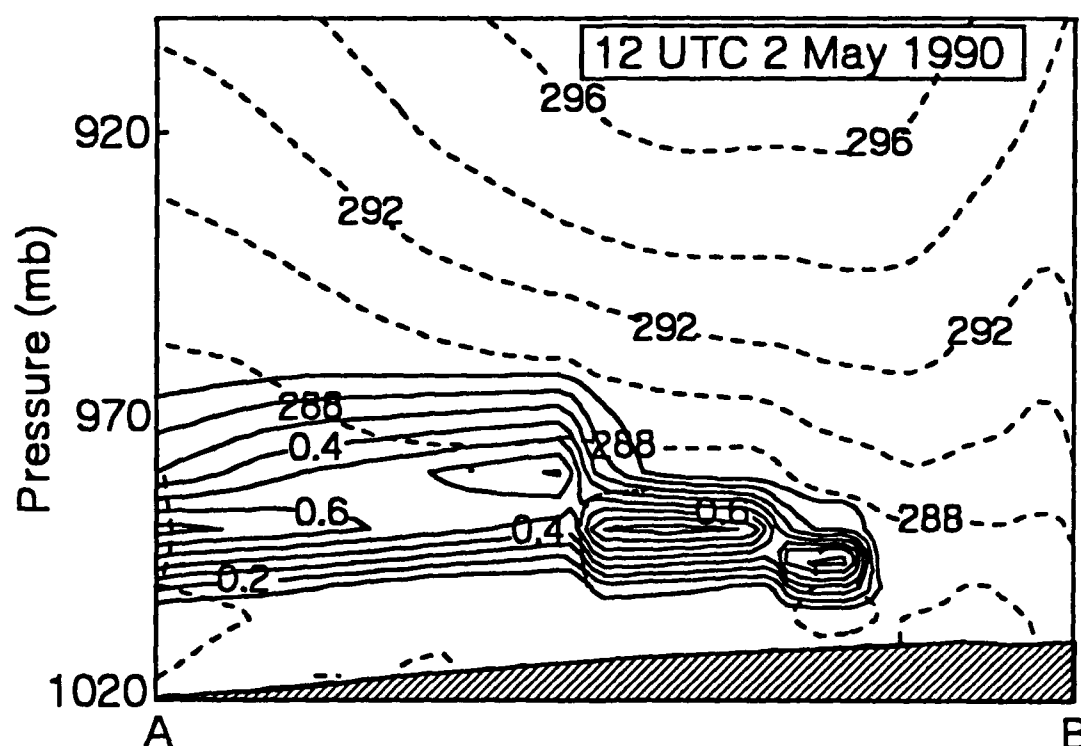
Figure 28. Cross section of Potential Temperature (K) and
Cloud Fractions: (solid; cloud fraction, dashed;
potential temperature), 1200 UTC 02 May 1990

Figure 29 is a profile of longwave cooling as related to the cloud fractional profile at point C just off the coast of northern California in which as noted in Chapter IV, a low pressure system is advancing. The upper level cirrus associated with the progress of this system is seen between 400mb and 250mb. Note the longwave cooling associated with this upper level cloud layer is significantly less due to the lower liquid water content. Additionally at the upper levels small amounts of longwave warming are seen. This warming is suggested to be caused by the thick layer of ozone located in the tropopause just above this cloud layer, which emits longwave radiation into the upper clouds and is absorbed.

The mid-level clouds between 850mb and 550mb appear similar to the low level clouds; however, the rate of longwave cooling is much less due to the lower liquid water content.
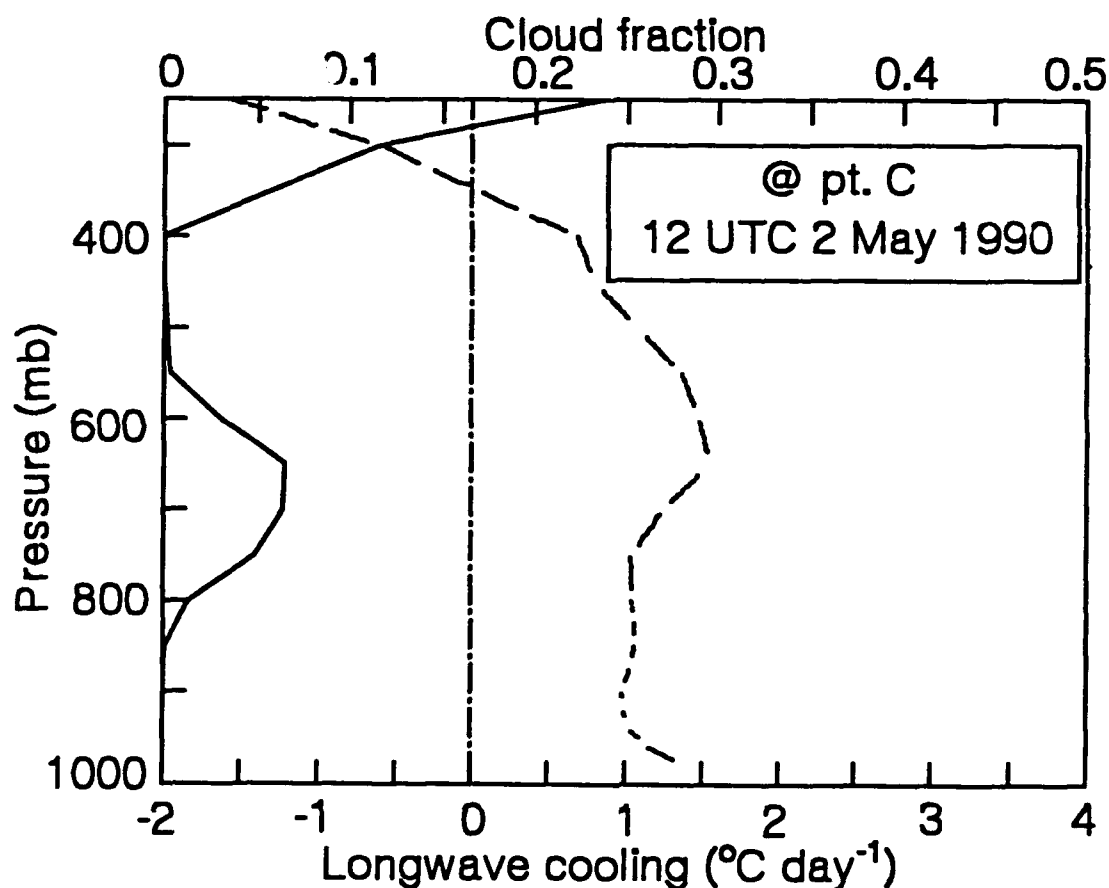
Figure 29. Profile of Longwave Cooling (°C/day) and Cloud
Fractions: (solid; cloud fraction, dashed;
longwave cooling), 1200 UTC 02 May 1990

The longwave cooling rates observed in the thin layer at the low level cloud tops are large, though not unreasonable. Kao and Yamada (1989) used a one dimensional model with high vertical resolution in the cloud layer to achieve cloud top cooling rates of 300 - 400°C per day. A simple test with a one dimensional version of the Harshvardhan (1987) radiation code was performed to illustrate the effects of cloud layer thickness and height on cooling rates.

Cloud layers were specified to correspond to various heights and thickness in the model's domain. Additionally, the effects of the model's vertical resolution on the calculation of the cooling rates of cloud tops were examined. Cloud top cooling rates of 50°C to 75°C per day were obtained for low level clouds. Estournal and Guedalia

(1985) demonstrated nocturnal cloud top cooling rates to be a function of the strength of the inversion layer and depth of the turbulent layer. The low level (1000mb-960mb) clouds in association with the longwave cloud top cooling rates seen in Figures 26 and 27 support this finding in the vicinity of the inversion.

d. Shortwave Warming

The introduction of shortwave radiation into the RAD model integration did not have the dramatic effect of longwave cooling; however, evidence of expansion of the cloud layers and atmospheric warming is seen.

Figure 30 is a cross section between points A and B of the shortwave warming in the lower atmosphere at 0000 UTC 03 May. The local maxima occur within the cloud and at ground level. The strong horizontal gradient at 900 mb is the vertical effect of the lower level clouds on the atmosphere above them. Figure 31 is a vertical profile at point D of shortwave warming throughout the atmosphere. Shortwave warming rates vary between 1°C and 4°C per day. As expected shortwave warming is highest in the cloud layers and at the surface.
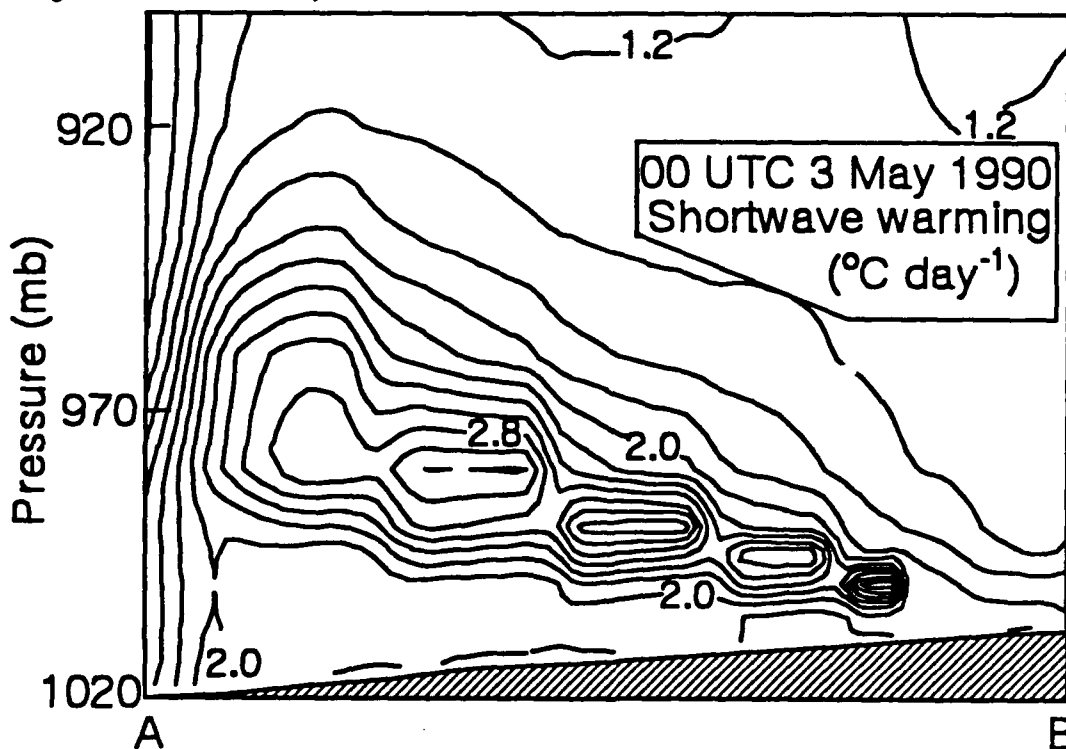

Figure 30. Cross Section of Shortwave Warming (°C/day): 0000 UTC 03 May 1990
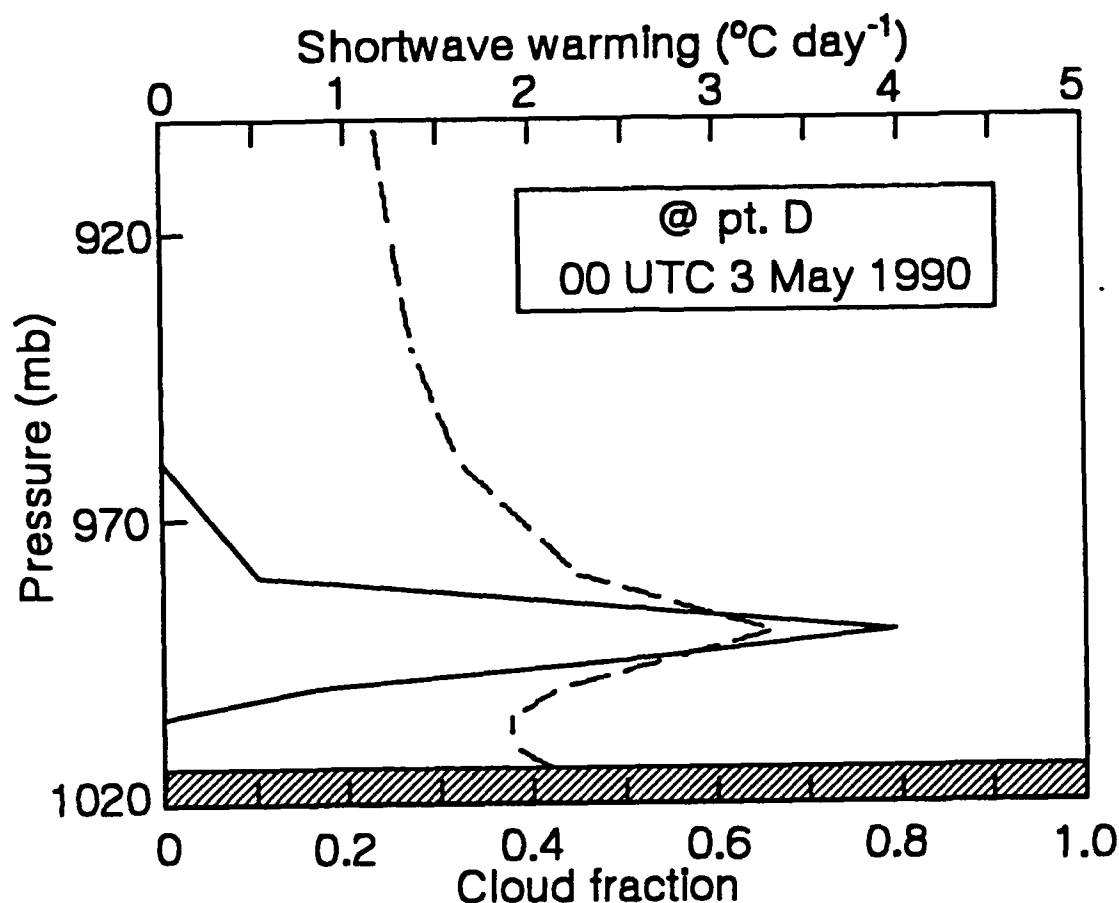
42

Figure 31. Profile of Shortwave Warming (°C/day) and Cloud Fractions: (solid; cloud fraction, dashed; shortwave cooling), 0000 UTC 03 May 1990

As can be seen from the temperature profiles, the shortwave radiation did not have a significant effect within or above the cloud layers, simply because of the magnitude of longwave cooling; however, if the temperature profiles from 1200 UTC 02 May and 0000 UTC 03 May are compared, the atmospheric warming can be seen. Figure 32 is the RAD model temperature profiles of the 1200 UTC 02 May and the 0000 UTC 03 May model runs at point D. Warming occurs in the cloud free atmosphere above the cloud layers. In this region longwave cooling is near zero.
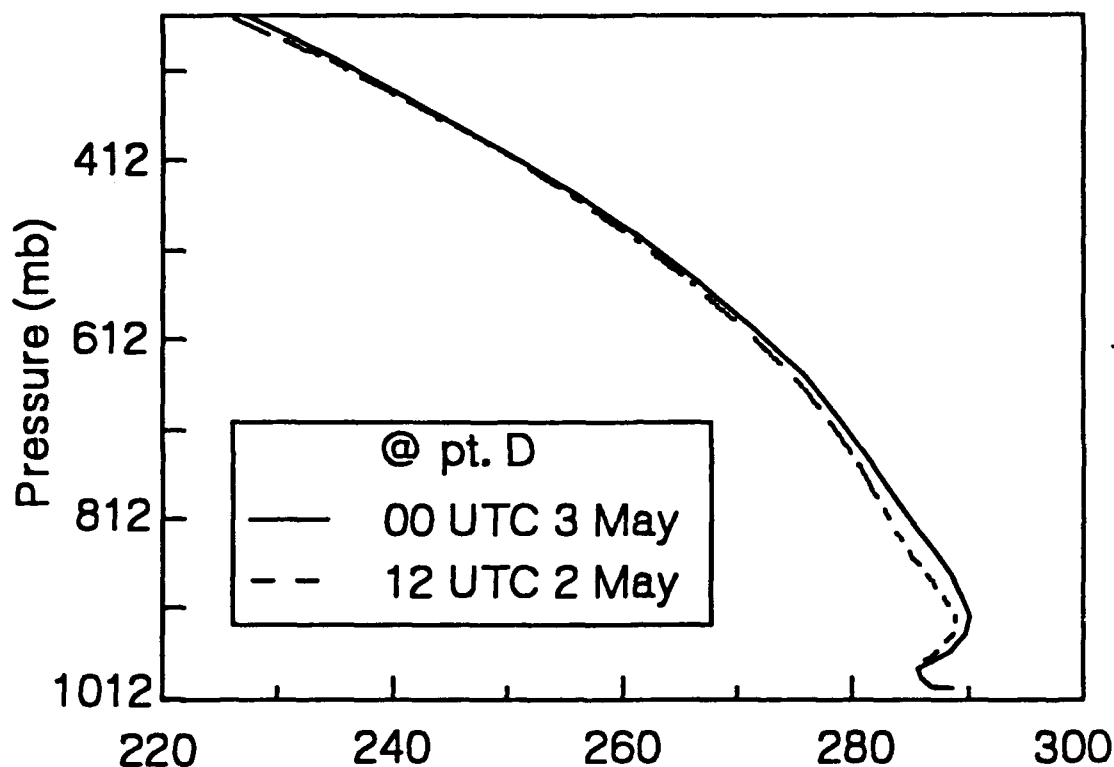
Figure 32. **Profile of Temperature (K):** (solid; 0000 UTC, dashed; 1200 UTC)

e. *Cloud Fractions*

The major reason for differences between the two model runs is the inclusion of the cloud parameterization in the RAD model. As discussed previously the longwave cooling associated with the cloud tops is significant; thus, the clouds generated in the RAD model require further examination.

Figure 33 is the cross section of cloud fractions from point A to point B at 0000 UTC 03 May. The vertical and horizontal structure of this stratus layer may be observed and is fairly constant throughout the 36 hour model integration. Figures 34 - 37 are the horizontal plots at 0000 UTC 03 May of the cloud structure in the southwestern quadrant of the model domain. Figures 38 - 40 are the horizontal plots of the mid-level cloud structure in the northwestern quadrant. These two cloud features are significant when validated against the 0000 UTC satellite imagery which support the existence of the low and upper level cloud structures observed.
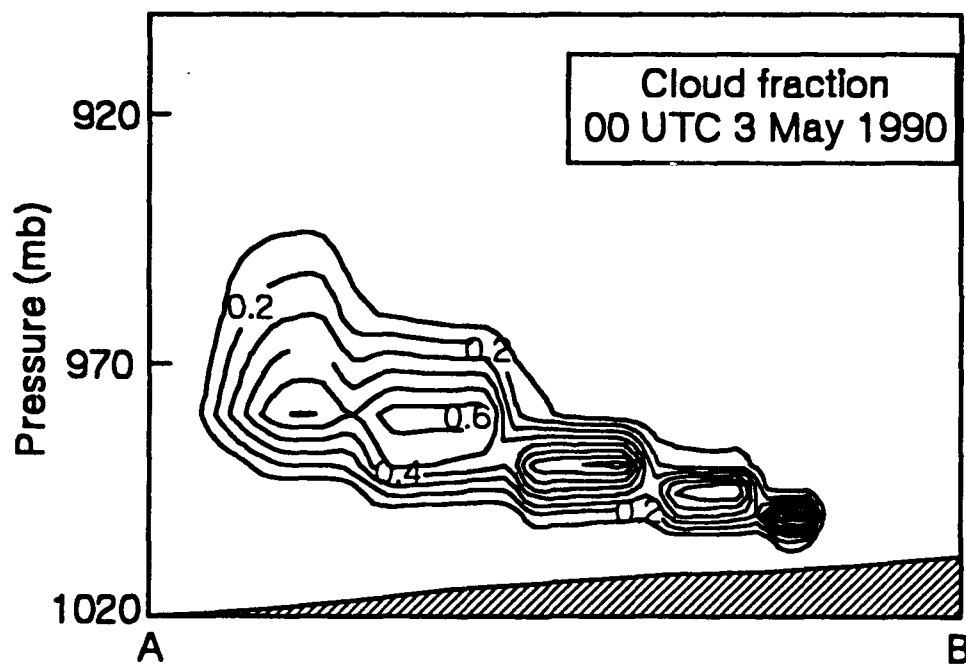
Figure 33. Cross Section of Cloud Fractions: from point A to point B, 0000 UTC 03 May 1990

Figure 34. 1000mb Cloud Fractions: 0000 UTC 03 May 1990

Figure 35. **995mb Cloud Fractions:** 0000 UTC 03 May 1990

Figure 36. **990mb Cloud Fractions:** 0000 UTC 03 May 1990

Figure 37. 980mb Cloud Fractions: 0000 UTC 03 May 1990
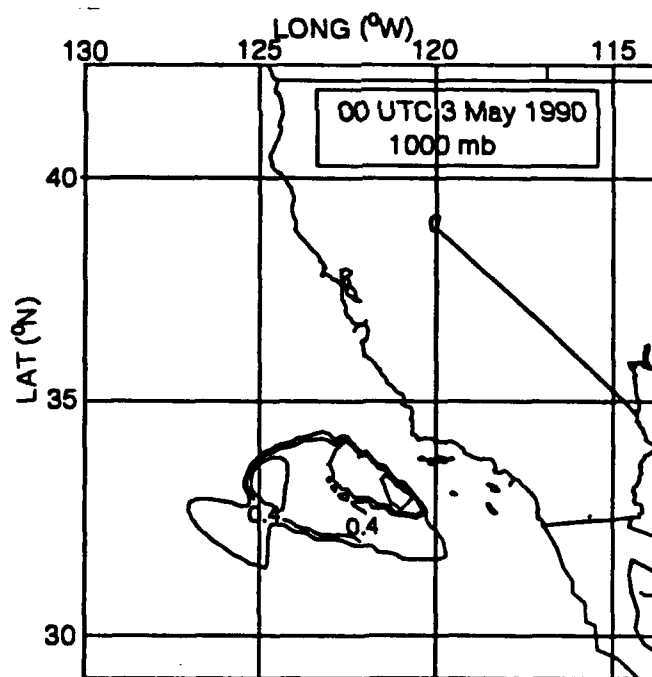

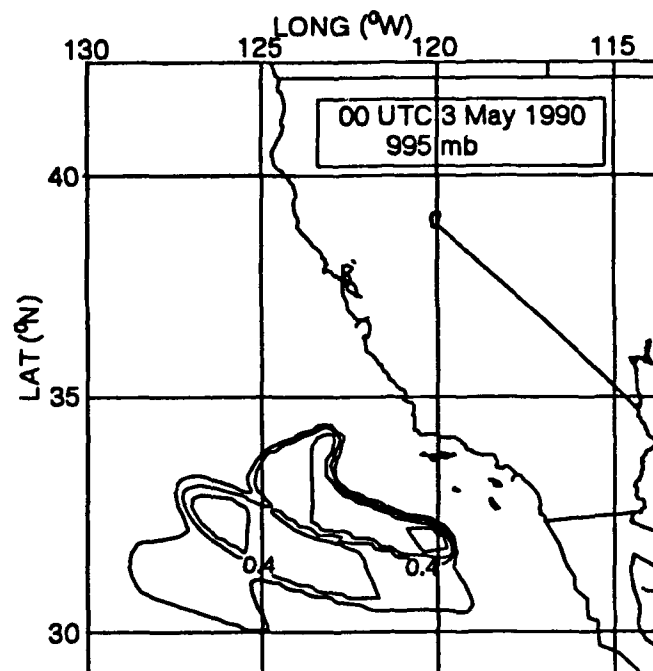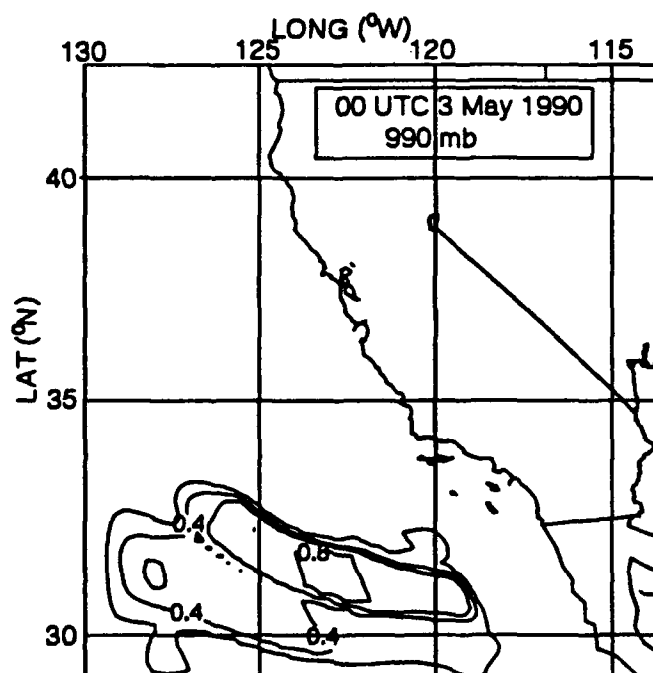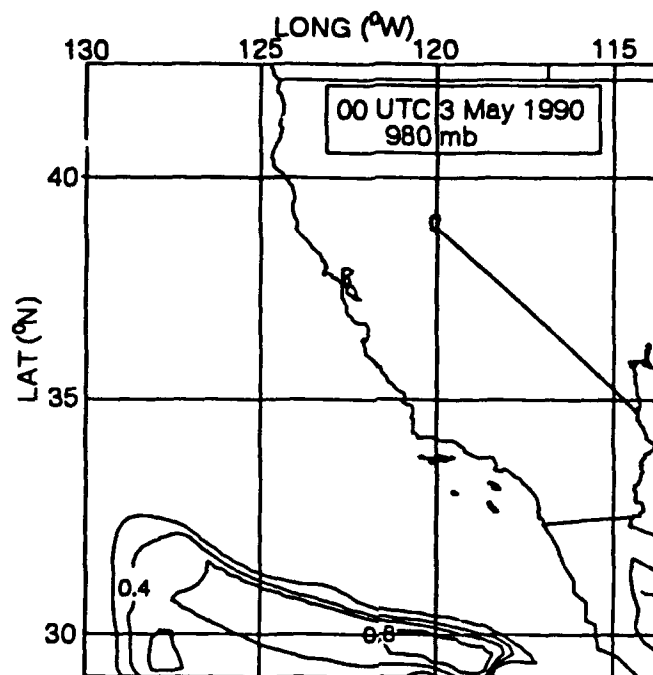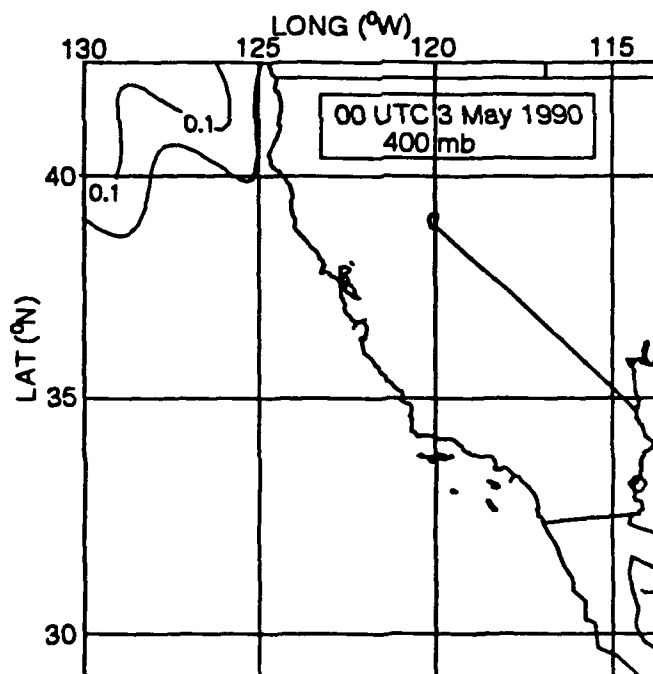**Figure 38.** 400mb Cloud Fractions: 0000 UTC 03 May 1990

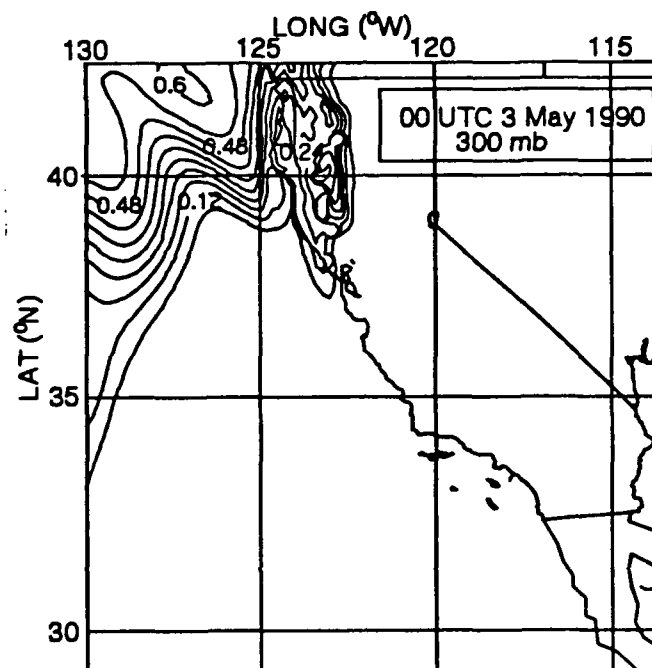Figure 39.   300mb Cloud Fractions: 0000 UTC 03 May
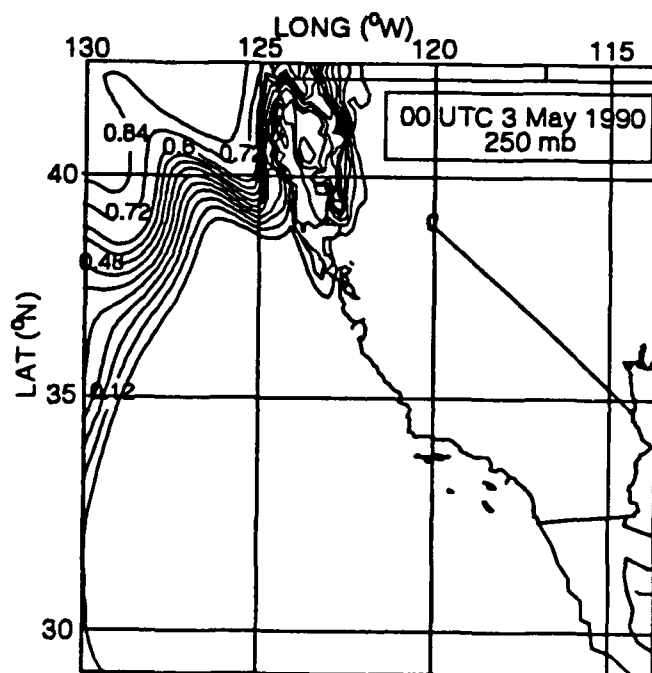   1990

Figure 40.   250mb Cloud Fractions: 0000 UTC 03 May
             1990

48

f. Precipitation

Precipitation was observed during the 36 hour integration of the RAD model from stable layer and convective clouds. Total accumulation from 0000 UTC 02 May to 1200 UTC 03 May was 0.25cm. A minimal amount of stable layer precipitation was observed in the low level clouds in the southern area of the domain. Based on the layer temperatures this precipitation was in the form of rain. The only convective precipitation occured in the mountainous regions between 1800 UTC and 0000 UTC which is consistent with satellite imagery. The amount of precipitation was restricted to less than 1cm for the six hours in which it occured. This precipitation and convective activity was not modeled by the CONTR model.

All convective activity occurred between 1800 UTC 02 May and 0000 UTC 03 May. Most of this convective motion may be seen in the satellite imagery; however, some smaller areas are not observed. The RAD model approximated convective activity only in the mountainous areas of the model domain and as seen in imagery, that is as expected in the western United States. Figure 41 is a horizontal plot of the convective areas as approximated by the convective precipitation areas with a contour interval of 0.25cm. Associated with this activity was minimal precipitation.
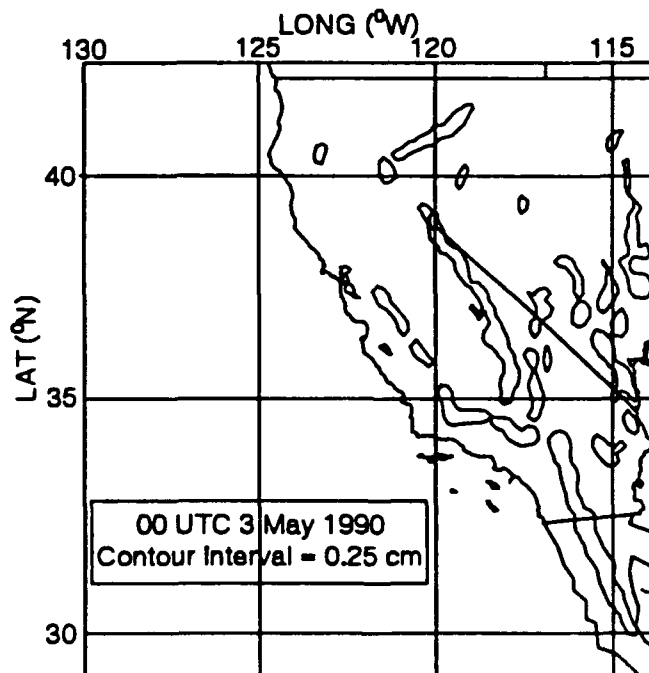

Figure 41.   Convective Precipitation Areas: 0000 UTC 03 May 1990

49

B. MODEL PERFORMANCE FOR MESOSCALE FEATURES

1. General

The introduction of the Harshvardhan et al. (1987) radiation parameterization was proposed in order to provide a more accurate simulation of the synoptic and mesoscale situations. The synoptic scale performance has been discussed previously and it has been shown in prior studies that synoptic scale patterns result in the mesoscale phenomena that are observed (Stephens et al., 1996). Therefore, three mesoscale features which have been documented during the period of this study have been closely evaluated to comprehend the RAD model's response to radiative effects, as compared to the CONTR model performance. The three mesoscale phenomena evaluated in this study as documented by Streed (1990), Corkill (1991), and Grandau (1992) are the sea and land breeze, the southerly surge, and the Catalina eddy, respectively.

2. The Sea and Land Breeze

As discussed previously, the nocturnal cooling offshore during the first 12 hour period was the major difference noted between the two models. This cooling resulted in a decreased low level temperature gradient across the land-marine boundary. This decreased gradient would normally result in a decreased flow of mass across the land-marine boundary, i.e., a change in the land breeze; however, as seen in previous studies (Grandau, 1992), the topographic features along the west coast of the United States often limit the areas of potential land breezes. One of these areas is the Salinas River valley where the NPS profiler site is located (Figure 19). Comparing the u and v wind components of the RAD and CONTR models yielded no significant difference between the two, suggesting the 1 - 2°C offshore temperature differences observed in the RAD model had negligible effect on the land breeze at 1200 UTC 02 May and 1200 UTC 03 May.

Figure 42 is the 1000mb u-component wind difference of the RAD - CONTR models at 1200 UTC 02 May. A negative number indicates weaker westerly components in the RAD model. This figure shows the offshore westerlies in the RAD model have been decreased in the area south of latitude 38°N by .5 - 2.0 m/s. This change in the wind pattern is a result of the high pressure ridge building which tends to create a weaker pressure gradient across the land - marine boundary. Figure 43 is the RAD sea level pressure (SLP) field at 1200 UTC 02 May. The shaded area in Figure 43 indicates SLP differences (RAD - CONTR) greater than 1mb. The low level cooling associated with this ridge generates pressure rises in the area near the California coast. The westerly components of the wind are decreased by the increased pressure region to the east.
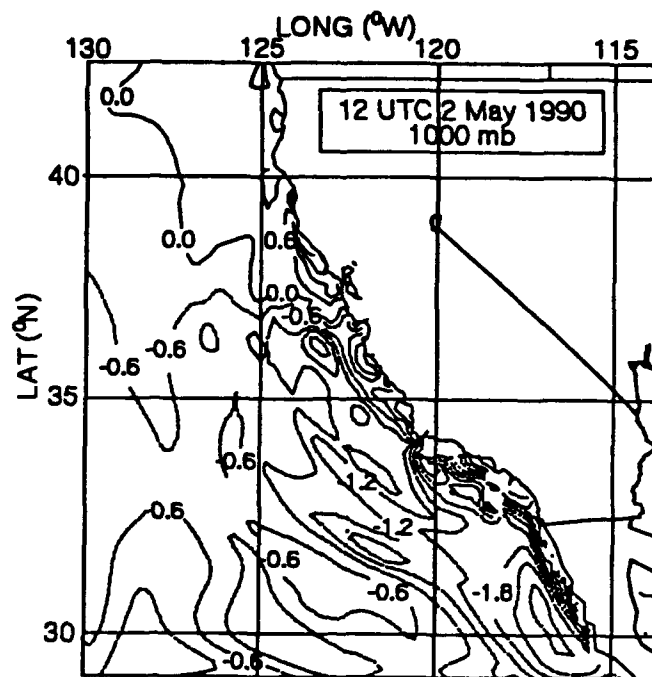
50

Figure 42.   1000mb u-Component Wind Difference Between
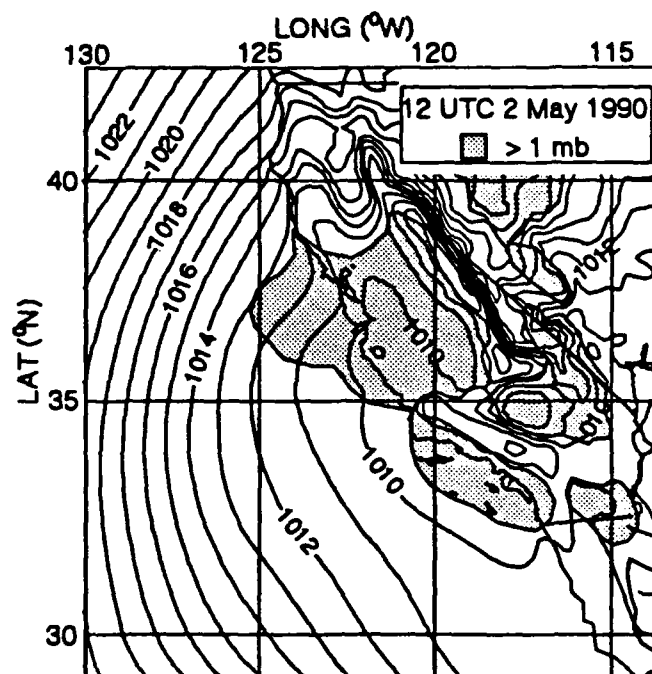RAD and CONTR Models: 1200 UTC 02 May
1990

Figure 43. Sea Level Pressure (mb) for Model RAD: 1200 UTC 02 May 1990;The shaded region indicates RAD-CONTR SLP differences greater than 1mb.

Figure 44 is the RAD - CONTR 1000mb u-component wind difference field at 0000 UTC 03 May. As before, a negative value indicates that the westerly wind component modeled by the RAD model is weaker than that modeled by the CONTR model.

Notice in the region 250km from the coast and seaward, weakened westerlies are the dominant feature, a result of the increased sea level pressures offshore in the RAD model (Figure 45). Figure 45 shows these surface pressure rises between the RAD and CONTR models. The strengthened westerlies (onshore) observed south of San Francisco Bay (37°N) are the result of two forces working together. First, the ridge building into the L.A. basin tends to turn the northwesterly flow toward the land north of the ridge axis, resulting in a slightly stronger westerly component of the wind. Second, the shortwave heating of the land throughout the daylight hours has assisted in setting up an afternoon sea breeze along the coast which is slightly stronger than that seen in the CONTR model. The 1200 UTC 03 May results are similar to those seen at 1200 UTC 02 May and will not be discussed.
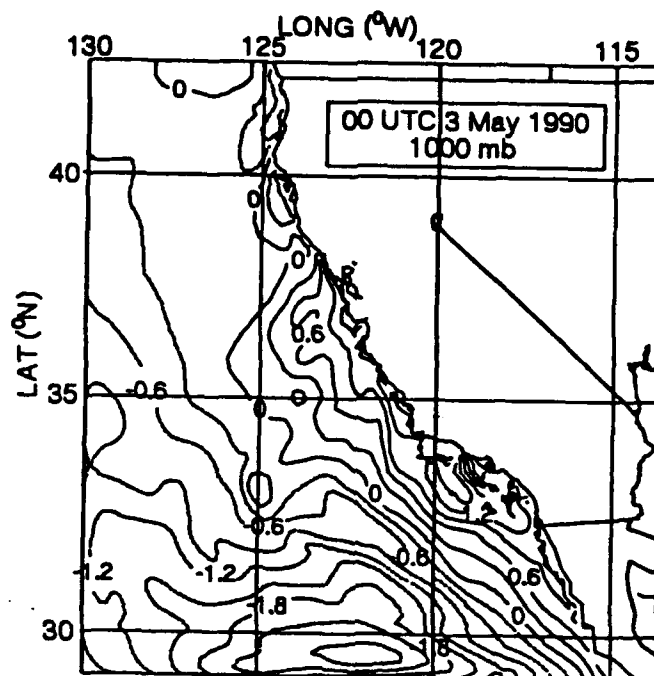
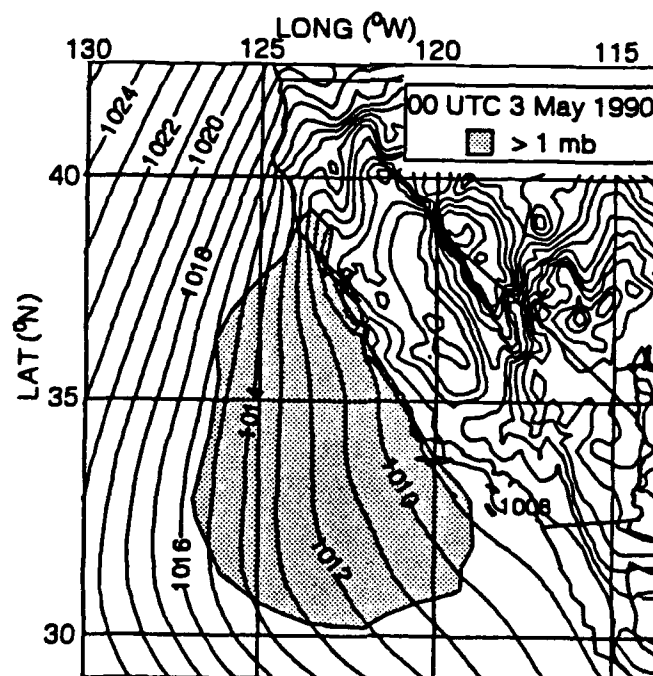**Figure 44.** 1000mb u-Component Wind Difference Between RAD and CONTR Models: 0000 UTC 03 May 1990

Figure 45. Sea Level Pressure for Model RAD: 0000 UTC 03 May 1990

3. The Southerly Surge

The mesoscale trough responsible for the southerly surge remains near the coast at 1200 UTC 02 May and the southerly flow is still observed but altered. Figure 46 is the RAD - CONTR 1000mb v-component wind difference field at 1200 UTC 02 May. A positive value indicates that the RAD model generates a weaker northerly flow compared to the CONTR model. The positive values along the coast indicate a broad area of weakened northerly flow. This is the result of the increased pressure region due to the low level longwave cooling. As the high pressure ridge continues to build, (Figure 43) we observe generally weaker flow throughout the model domain except for a small region south of 32°N extending to 750km offshore. This region of increased northerly flow is south of the ridge axis where the pressure gradient is from high (ridge) to low.

The southerly surge was observed between Ensenada, MX (31°N) and Los Angeles (34°N) in the RAD model. In this area the southerly surge was subject to perturbations in the southerly flow due to the ridge structure along the coast. As seen in Figure 46, the forces brought on by the ridging resulted in a .5 - 2.0 m s increase in the southerly component of the southerly surge north of San Diego while south of San Diego a .5 - 1.0 m s decrease in the southerly flow was observed. This is a very positive result, as the CONTR model approximated winds 2.0 m s below the observed southerly surge during this time period.

Figure 46. 1000mb v-Component Wind Difference Between RAD and CONTR Models: 1200 UTC 02 May 1990

Figure 47 is the RAD - CONTR 1000mb v-component wind difference fields at 0000 UTC 03 May. Due to the pressure increases (Figure 45), we observe a broader area of weakened northerly flow. As observed at 1200 UTC 02 May, the RAD model generates a similar response to the high pressure ridging in the southeast with weakened northerly flow north of the ridge axis and strengthened northerly flow south of the axis.

At 0000 UTC 03 May, the RAD model forecast a weaker southerly surge between Los Angeles and Ensenada, MX than CONTR. It is observed in Figure 47, that the entire region of the southerly surge is contained within the strengthened northerly flow as approximated by the RAD model. This indicates a .5 - 1.0 m/s decrease in the southerly surge modeled by the RAD model. Thus the RAD model provides a more accurate forecast of the diurnal evolution of the southerly surge.
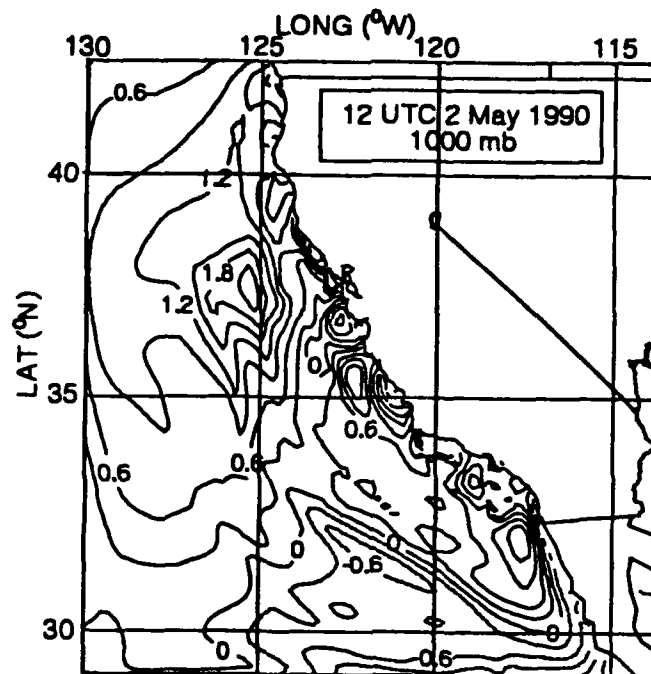
Figure 47. 1000mb v-Component Wind Difference Between RAD and CONTR Models: 0000 UTC 03 May 1990

Figure 48 is the RAD - CONTR 1000mb v-component wind difference field. As observed in the previous two 12 hour periods, the high pressure ridging has deformed the northerly flow pattern with weakened northerly flow north of the ridge axis and strengthened northerly flow to the south of the ridge axis. As mentioned previously, these changes are due to the high pressure ridging and the pressure gradient asociated with it. Figure 49 is the RAD sea level pressure field at 1200 UTC 03 May similar to Figure 43 which shows the stronger and broader area of higher pressures offshore modeled by RAD.

The southerly surge approximated by the RAD model at 1200 UTC 03 May is located between Los Angeles and Ensenada, MX. North of San Diego the southerly surge is greater than the CONTR model by .5 - 1.0 m/s, south of San Diego, it is less than the CONTR model by .5 - 1.0 m/s. This result at both the 1200 UTC observations is very positive as the southerly surge is accelerated in the Catalina basin. Grandau (1992) noted that the CONTR model forecasts of the southerly surge were 2.0 m/s weaker than the observed values; thus, the RAD model represents a substantial improvement in the area of the southerly surge. The increase in the southerly flow as dis-

56

cussed in Chapter IV, leads to the topographically forced Catalina eddy and will be examined next.
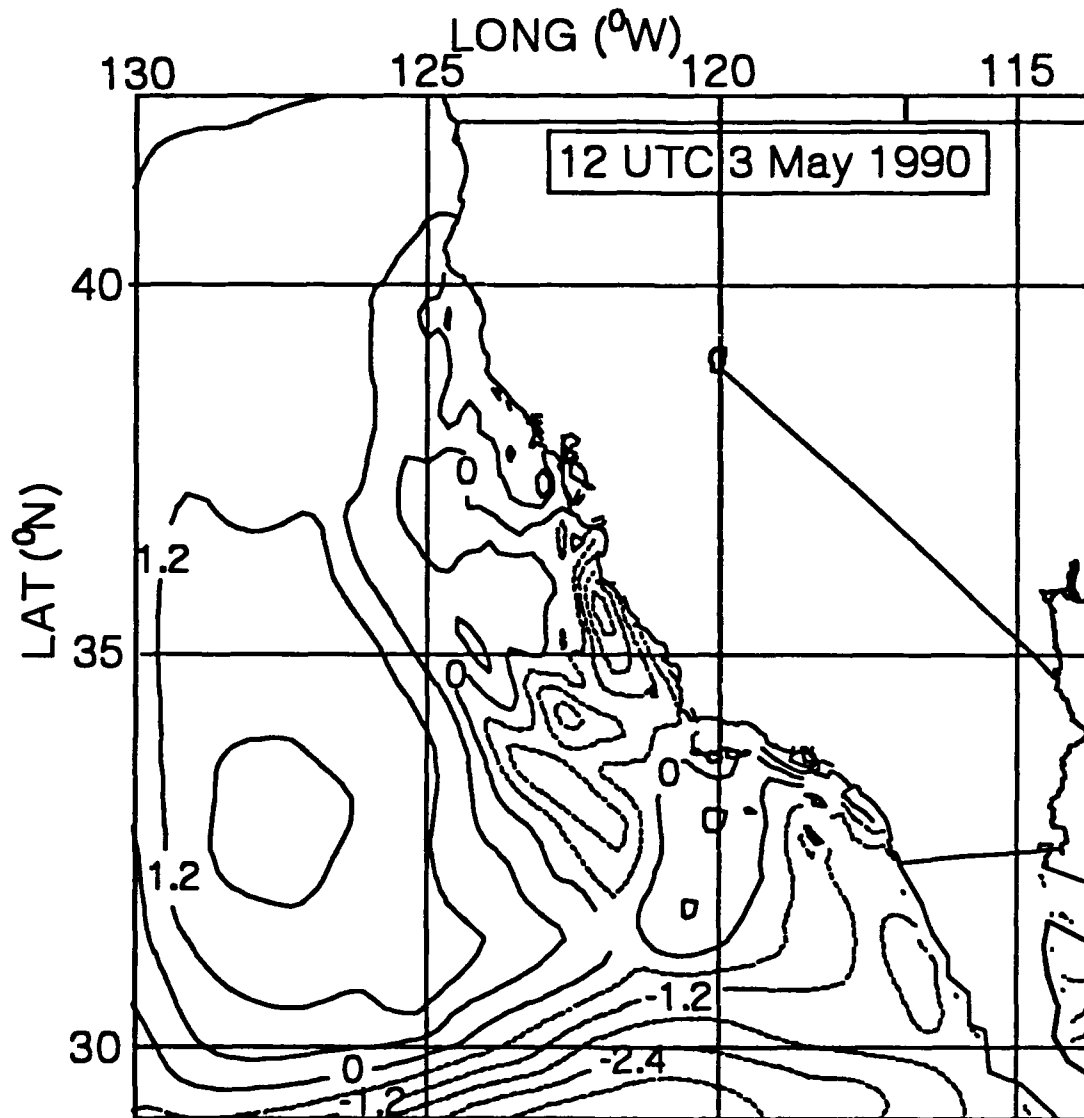

Figure 48. 1000mb v-Component Wind Difference Between RAD and CONTR Models: 1200 UTC 03 May 1990

Figure 49. Sea Level Pressure (mb) for Model RAD: 1200 UTC 03 May 1990

4. Catalina Eddy

One of the major differences between the RAD and CONTR models is the evolution of the Catalina eddy. The RAD model from the onset of the integration (0000 UTC 02 May 1990) indicated lower geopotential heights, a strengthened southerly surge at 1200 UTC daily and a high pressure ridge forming along the coast which all seemed to provide additional forcing to spin up the eddy rapidly. The eddy shows signs of strong development at 6 hours into the model integration and by 12 hours is a well defined phenomena from the surface to 920mb, as also simulated in CONTR. Figure 50 is a horizontal plot of the RAD model 1000mb wind field at 1200 UTC 02 May. By 1800 UTC 02 May, the eddy has begun to weaken and by 0000 UTC 03 May the eddy is completely disjointed (Figure 51).

As discussed earlier, in the last 12 hours of the RAD model integration (1200 UTC 03 May) a stronger southerly surge is generated in the Los Angeles - Catalina region than in the CONTR simulation. An increased southerly flow would normally enhance the spin up of the Catalina eddy; however, the Catalina eddy was not observed in the RAD model but was in the CONTR model (Figure 52).

58

The ridge which is forming along the coast throughout the model integration is a positive result, yet it did not provide a strong enough southerly surge combined with the other forces to spin up the eddy at 1200 UTC 03 May. The RAD 1200 UTC 03 May sea level pressure field (Figure 49) denoted the weak ridging area just west of the channel islands. The CONTR model which lacked this ridging approximated a 1.5 - 2.0 m/s stronger westerly wind component than the RAD model due to offshore troughing in the L.A. basin area. If the ridge were better established to force a stronger southerly surge the RAD model should also develop a Catalina eddy in the last 12 hours of the model integration as the observations indicate.
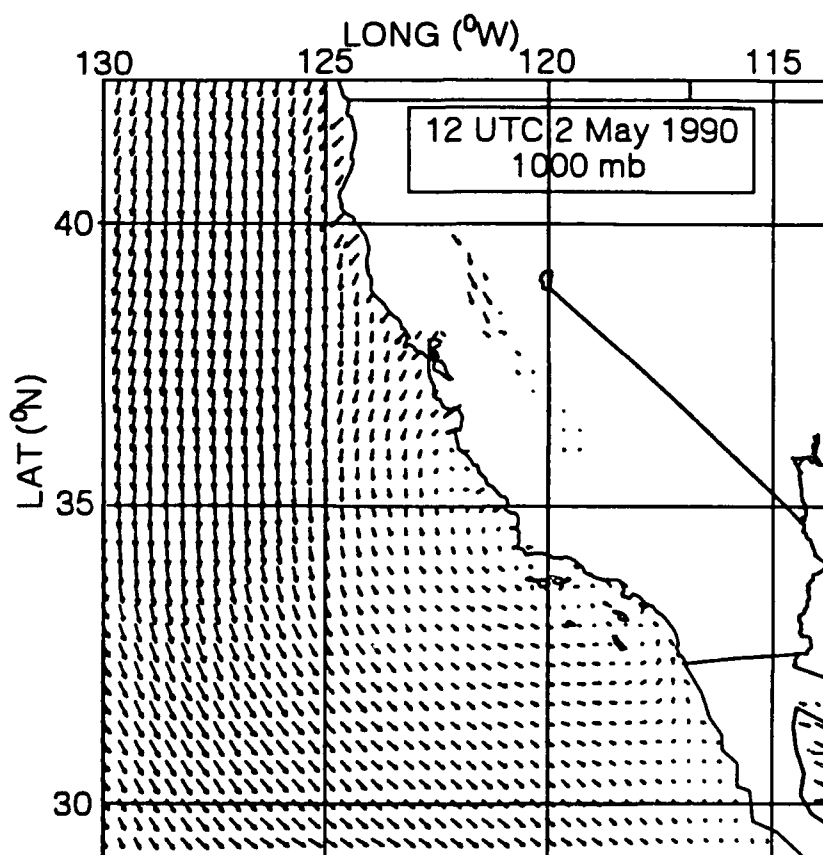

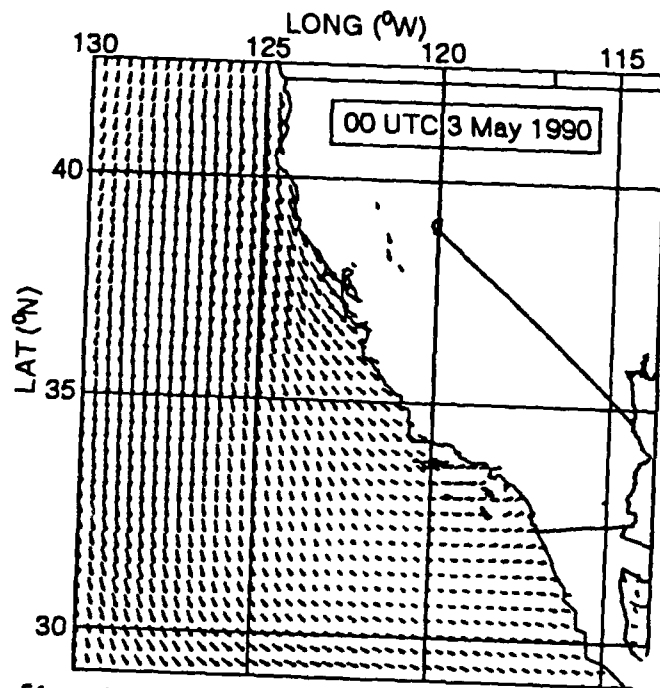**Figure 50.   1000mb Wind Field: 1200 UTC 02 May 1990,**
RAD Model

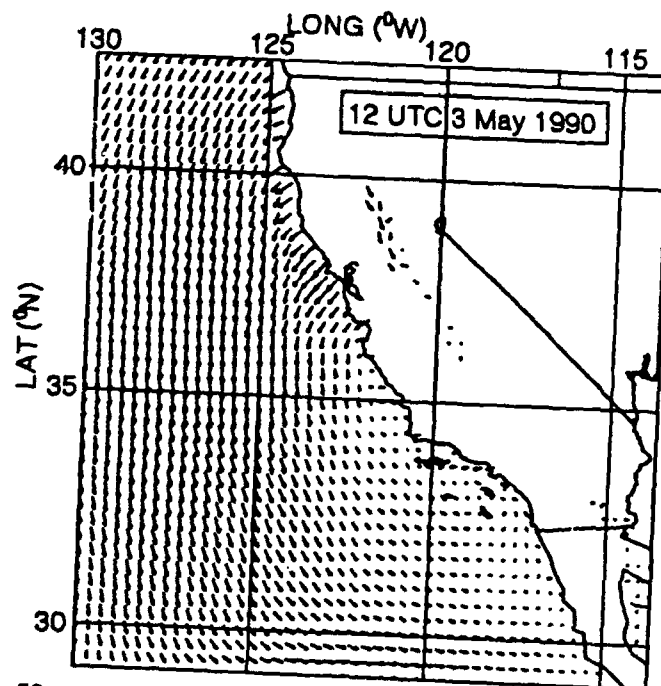**Figure 51.** **1000mb Wind Field:** 0000 UTC 03 May 1990, RAD Model

Figure 52. **1000mb Wind Field:** 1200 UTC 03 May 1990, CONTR Model

VI. CONCLUSIONS AND RECOMMENDATIONS

A. CONCLUSIONS

This study has shown that the incorporation of the Harshvardhan et al. (1987) radiation parameterization scheme into the NRL model is a positive improvement in the simulation of the eastern Pacific oceanic region. Specifically, the shortwave and longwave radiation represents a substantial improvement in the model's ability to replicate the diurnal and cloud related radiative processes. As verified by satellite imagery, the cloud fractions generated are accurate; however, limitations exist.

The comparison of the two models in their reaction to approximating three mesoscale phenomena; the sea and land breeze, the southerly surge, and the Catalina eddy, resulted in some very interesting conclusions. In the case of the sea and land breeze, the RAD model u and v wind components differ significantly from the CONTR model due to building of a high pressure ridge along the coast as was suggested in the observations; however, in comparing profiler data the land breeze did not significantly differ from the CONTR model. The sea breeze effects modeled in the RAD model appeared stronger; however, on closer examination the differences were attributed to the ridge forming in the area off San Diego and the turning of the northwesterly flow as well as the shortwave heating of the land. Additionally, as observed in the other mesoscale phenomena it depended where the mesoscale feature occured in relation to the high pressure ridging to determine its' effect on the feature.

The southerly surge, much like the sea and land breeze, was subject to many changes in its' evolution due to the ridge formation. This reaction resulted in perturbations of the diurnal southerly surge along the California coast as the horizontal, mesoscale structure of the the geopotential height fields varied. The southerly surge modeled by Grandau (1992) in the CONTR model was 2-4 m/s weaker than the observations. In the first 12 hours of the RAD model simulation, an improvement was made as the southerly surge was accelerated by 2 m/s. This improvement was again observed at 1200 UTC 03 May suggesting the diurnal forcings associated with the southerly surge were better modeled by the RAD model.

The Catalina eddy was subject to the same interactions as the previous two phenomena in that the offshore ridge affected its' formation. The southerly surge was more accurately approximated by the RAD model; however, it was insufficiently strong

enough to properly influence the evolution of the Catalina eddy in the last 12 hours of the model run. This result was attributed to the weaker onshore flow modeled during this period reinforcing the interconnection of the southerly surge and the Catalina eddy examined here.

B. RECOMMENDATIONS

Grandau (1992) and this study noted shortcomings in the model's simulation of specific humidity fields. To examine these shortcomings, a comparison of the model simulated horizontal and vertical relative humidity structure to the observed satellite cloud patterns was made. Compared to the Slingo (1985)scheme, the model generated relative humidity profile was generally too limiting for cloud generation in the lower levels. For example, in Figure 53 at 1000mb in the vicinity of 30°N, 125°W, the RAD model generated a relative humidity of less than 96%, compared to a critical value of 100% for cloud generation but satellite imagery indicated that low level clouds were present.

A modification to the critical relative humidity of Slingo (1985) is provided here for further research of the 2-3 May 1990 case study. The modification is based on matching model generated relative humidity profiles to observed satellite cloud structure. The empirical equation (3.1) was linearly modified to provide a profile of critical relative humidities in the lower levels necessary for clouds to form in the model to coincide with those observed. This modification was based on satellite and analysis observations during the period of this study. Figure 54 is the profile of these modifications based on equations (6.1), (6.2), and (6.3). Note the low level slope diferences between the dashed line (modified) and the solid line (Slingo).

$$Rh_k^c = 1 + 2(\sigma_k^2 - \sigma_k) + \sqrt{3}\sigma_k(1 - 3\sigma_k + 2\sigma_k^2) \qquad (6.1)$$

$$for \ \sigma_k < 0.88$$

$$Rh_k^c = 1 + 2(\sigma_k^2 - \sigma_k) + \sqrt{3}\sigma_k(1 - 3\sigma_k + 2\sigma_k^2) + 1.03276(0.83179 - \sigma_k) \qquad (6.2)$$

$$for \ 0.88 \leq \sigma_k < 0.99$$

$$Rh_k^c = 1 + 2(\sigma_k^2 - \sigma_k) + \sqrt{3}\sigma_k(1 - 3\sigma_k + 2\sigma_k^2) - 11.726(1.00393 - \sigma_k) \qquad (6.3)$$

$$for \ \sigma_k \geq 0.99$$

Figure 53.   Relative Humidity at 1200 UTC 02 May 1990

Another area for further research is the model's ability to simulate moisture in the atmosphere.   The same shortcomings noted by Grandau (1992) are found in the RAD model; however, with the incorporation of a stratus parameterization the low and mid-level moisture pattterns will be better depicted.

The improved model, as it now stands, generates heating rates at each of the gridpoints in the model's 23 layers.   Verification of the rates is nearly impossible.   With the advent of remote sensing devices which will probe the atmosphere and insitu aircraft measurements, substantiation of these rates will be achievable.

Figure 54. Modified Critical Relative Humidity

REFERENCES

Arakawa, A., and V.R. Lamb, 1977: Computational design of the basic dynamic process of the UCLA general circulation model. *Methods in Computational Physics*, Vol. 17, Academic Press, 173-265.

Blackadar, A.K., 1976: Modeling of the nocturnal boundary layer. Preprints, *Third Symposium on Atmospheric Turbulence, Diffusion and Air Quality*, Raleigh, Amer. Meteor. Soc., 46-49.

Bosart, L.F., 1983: Analysis of a California eddy event. *Mon. Wea. Rev.*, 111, 1619-1633.

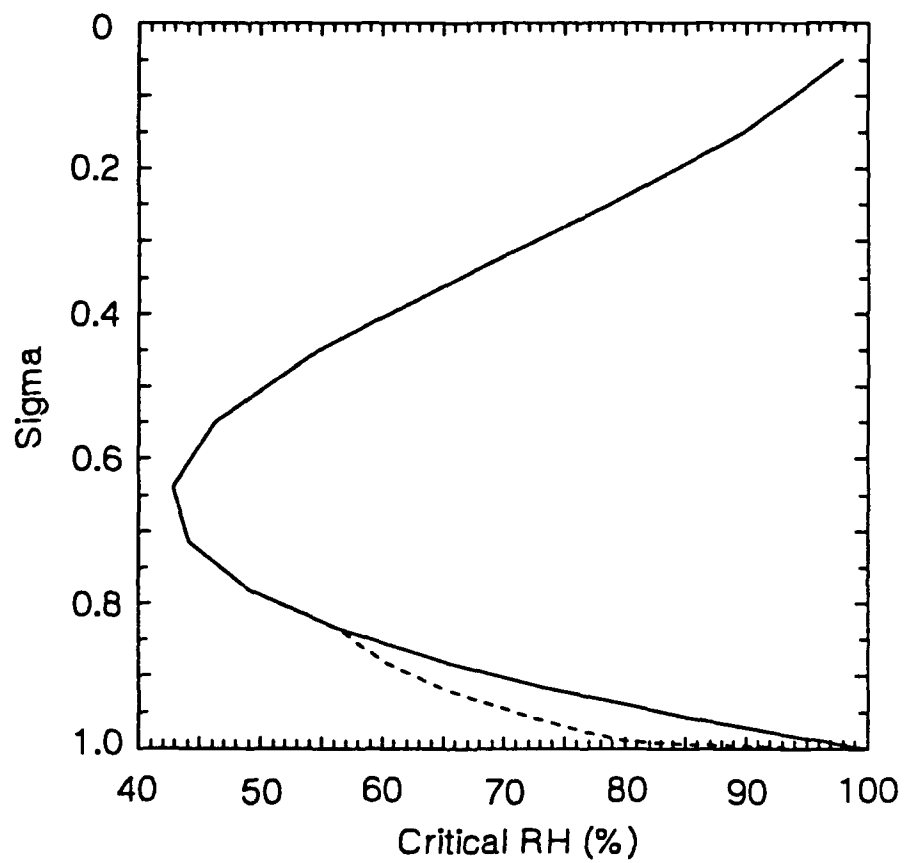Chang, S.W., 1979: An efficient parameterization of convective and non-convective planetary boundary layers for use in numerical models. *J. Appl. Meteor.*, 18, 1205-1215.

Chang, S.W., K. Brehme, R. Madala, and K. Sashegyi, 1989: A numerical study of the east coast snowstorm of 10-12 February 1983. *Mon. Wea. Rev.*, 117, 1768-1776.

Chou, M.D., and A. Arking, 1980: Computation of infrared cooling rates in the water vapor bands. *J. Atmos. Sci.*, 37, 855-867.

Chou, M.D. and L. Peng, 1983: A parameterization of the absorption in the $15\mu m$ CO_2 spectral region with application to climate sensitivity studies. *J. Atmos. Sci.*, 40, 2183-2192.

Chou, M.D., 1984: Broadband water vapor transmission functions for atmospheric IR flux computations. *J. Atmos. Sci.*, 41, 1775-1778.

Coakley, J.A., and P. Chylek, 1975: The two stream approximation in radiative transfer: Including the angle of the incident radiation. *J. Atmos. Sci.*, 32, 409-418.

Corkill, P.W., 1991: Synoptic and mesoscale factors influencing stratus and fog in the central California coastal region. M.S. Thesis, Meteorology Department, Naval Postgraduate School, Monterey, CA 93943.

Dorman, C.E., 1985: Evidence of Kelvin waves in California's marine layer and related eddy generation. *Mon. Wea. Rev.*, 113, 827-839.

Estournal, C., and D. Guedalia, 1985: Influence of geostrophic wind on atmospheric nocturnal cooling. *J. Atmos. Sci.*, 42, 2695-2698.

Grandau, F.J., 1992: Evaluation of the Naval Research Laboratory limited area dynamical weather prediction model: topographic and coastal influences along the

west coast of the United States. M.S. Thesis, Meteorology Department, Naval Postgraduate School, Monterey, CA 93943.

Haltiner, G.J., and F.L. Martin, 1972: Dynamical and Physical Meteorology, McGraw-Hill, Inc., 52.

Hansen, J.E., G. Russel, D. Rind, P. Stone, A. Lacis, S. Lebedeff, R. Ruedy, and L. Travis, 1983: Efficient three-dimensional global models for climate studies: Models I and II. *Mon. Wea. Rev.*, **111**, 609-662.

Harrison, E.F., P. Minnis, B.R. Barkstrom, V. Ramanathan, R.D. Cess, and G.G. Gibson, 1990: Seasonal variation of cloud radiative forcing derived from the Earth Radiation Budget Experiment. *J. Geophys. Res.*, **95**, 18687-18703.

Harshvardhan, and D.A. Randall, 1985: Comments on "The parameterization of radiation for numerical weather prediction and climate models". *Mon. Wea. Rev.*, **113**, 1832-1833.

Harshvardhan, R. Davies, D.A. Randall, and T.G. Corsetti, 1987: A fast radiation parameterization for atmospheric circulation models. *J. Geophys. Res.*, **92**, 1009-1016.

Holt, T., and S. Raman, 1988: A review and comparitive evaluation of multi-level boundary layer parameterizations for first order and turbulent kinetic energy closure schemes. *Rev. Geophys.*, **26**, 761-780.

Holt, T., S. Chang, and S. Raman, 1990: A numerical study of coastal cyclogenesis in Gale IOP-2: Sensitivity to parameterizations. *Mon. Wea. Rev.*, **118**, 234-257.

Joseph, J.H., W.J. Wiscombe, and J.A. Weinman, 1976: The delta Eddington approximation for radiative flux transfer. *J. Atmos. Sci.*, **33**, 2452-2459.

Kuo, H.L., 1974: Further studies of the parameterization of the influences of cumulus convection on large-scale flow. *J. Atmos. Sci.*, **31**, 1232-1240.

Lacis, A.A., and J.E. Hansen, 1974: A parameterization for the absorption of solar radiation in the earth's atmosphere. *J. Atmos. Sci.*, **31**, 118-133.

Madala, R.V., S.W. Chang, U.C. Moharty, S.C. Madan, R.K. Paliwal, V.B. Sarin, T. Holt, and S. Raman, 1987: Description of the Naval Research Laboratory limited area dynamical weather prediction model. NRL technical Report 5992. [Available from NRL Washington DC 20375].

Mass, C.F., and M.D. Albright, 1989: Origin of the Catalina Eddy. *Mon. Wea. Rev.*, **117**, 2406-2436.

Morcrette, J.J., 1990: Impact of changes to the radiation transfer parameterizations plus cloud optical properties in the ECMWF model. *Mon. Wea. Rev.*, **118**, 847-873.

Ramanathan, V., E.J. Pitcher, R.C. Malone, and M.L. Blackmon, 1983: The response of a spectral general circulation model to refinements in radiative processes. *J. Atmos. Sci.*, **40**, 605-630.

Ritter, B. and J.F. Geleyn, 1992: A comprehensive radiation scheme for numerical weather prediction models with potential applications in climate simulations. *Mon. Wea. Rev.*, **120**, 303-325.

Roberts, R.E., J.E.A. Selby, and L.M. Biberman, 1976: Infrared continuum absorption by atmospheric water vapor in the 8-12μm window. *Appl. Opt.*, **15**, 2085-2090.

Rodgers, C.D., 1968: Some extention and applications of the new random model for molecular band transmission. *Quart. J. Roy. Meteor. Soc.*, **94**, 99-102.

Schmetz, J., E. Raschke, and H. Fimpel, 1981: Solar and thermal radiation in maritime stratocumulus clouds. *Contrib. Atmos. Phys.*, **54**, 442-452.

Schulz, W.J., 1992: Wind speed and moisture sensitivity tests of the NRL limited area dynamical weather prediction model: An OSSE study of ERICA IOP-4. M.S. Thesis, Meteorology Department, Naval Postgraduate School, Monterey, CA 93943.

Slingo, J.M., and B. Ritter, 1985: Cloud prediction in the ECMWF model. ECMWF Tec. Rep. No. 46, 48pp. [Available from The European Centre for Medium-Range Weather Forecasts, Shinfield Park, Reading RG2 9AX, U.K.].

Slingo, J.M., 1989: A GCM parameterization for the shortwave radiation properties of water clouds. *J. Atmos. Sci.*, **46**, 1419-1427.

Stephens, G.L., 1984: The parameterization of radiation for numerical weather prediction and climate models. *Mon. Wea. Rev.*, **112**, 826-867.

Stephens, G.L., and S.C. Tsay, 1990: On the cloud absorption anomaly. *Quart. J. Roy. Meteor. Soc.*, **116**, 671-704.

Streed, D.H., 1990: High-frequency meteorological phenomena observed with the Naval Postgraduate School's UHF Doppler wind profiler. M.S. Thesis, Meteorology Department, Naval Postgraduate School, Monterey, CA 93943

Wilson, C.A. and J.F.B. Mitchell, 1986: Diurnal variation and cloud in a general circulation model. *Quart. J. Roy. Meteor. Soc.*, **112**, 347-369.

World Meteorlogical Organization, 1984: The intercomparison of radiation codes in climate models (ICRCCM). *WCP-93*, 37 pp., Geneva.

INITIAL DISTRIBUTION LIST

No. Copies

1. Defense Technical Information Center   2
    Cameron Station
    Alexandria, VA 22304-6145

2. Library, Code 52   2
    Naval Postgraduate School
    Monterey, CA 93943-5002

3. Chairman (Code MR Hy)   1
    Department of Meteorology
    Naval Postgraduate School
    Monterey, CA 93943-5000

4. Chairman (Code OC Co)   1
    Department of Oceanography
    Naval Postgraduate School
    Monterey, CA 93943-5000

5. Professor Teddy R. Holt (Code MR Ht)   1
    Department of Meteorology
    Naval Postgraduate School
    Monterey, CA 93943-5000

6. Professor Roger T. Williams (Code MR Wu)   1
    Department of Meteorology
    Naval Postgraduate School
    Monterey, CA 93943-5000

7. Dr. Simon Chang   1
    Naval Research Laboratory Code 4220
    Washington, D.C. 20375

8. Dr. Chi-San Liou   1
    Naval Research Laboratory-Monterey
    Monterey, CA 93943-5006

9. Dr. Lee W. Eddington   1
    Geophysics Division
    Pacific Missile Test Center
    Point Mugu, CA 93042-5000

10. Dr. Gary Geernaert   1
    Office of Naval Research, Code 1122MM
    800 N. Quincy St.
    Arlington, VA 22217-5000

11. Dr. John Hovermale   1
    Naval Research Laboratory - Monterey
    Monterey, CA 93943-5006

12. LT Paul C. Stewart   2
    Naval Western Oceanography Center
    Box 113
    Pearl Harbor, HI 96860-5000